Development of a Micro-PIXE facility for analysis of geological samples

By

P.T.Mkhabela

BSc (Ed) University of North West

(1998)

Dissertation Submitted in Partial Fulfilment

of the Requirements for the Degree of

Master of Science

(Applied Radiation Science and Technology)

University of North West

July 2001

ABSTRACT

This work involved the development of a collimated micro-PIXE facility for analysis of geological samples. The old facility operated very well but there were problems encountered during its operation. The ion beam spot was found to have increased by a factor of two relative to the expected size. This was a beam halo that was formed around the beam. The beam halo problem was attributed to the collimator slit scattering, the length of the beamline and the vacuum level in the beamline.

The existing quadrupole lens system was very close to the target, therefore strong focussing had to be used to achieve the aimed beam spot of the size in the range of 50-80 microns at the target. A small variation of the focussing led to defocusing at the target, this was another factor leading to the observed beam halo.

A new beamline had to be developed to achieve a beamspot size in the range of 50-80 microns at the target. This was achieved by making the beamline longer and using three sets of collimators so as to produce a more parallel ion beam. A pair of quadrupole magnets was inserted about 300 cm from the collimators to gain more flexible control of the ion beam. This helped to reduce the beam halo by a considerable amount.

This work required the use of an ion accelerator, bending/analysing magnets, quadrupole magnets, vacuum system, collimators, detectors, software and

electronic equipment.

Quadrupole magnets were used to focus the beam before entering the collimators. When selecting collimators, careful consideration was devoted to the shape of the collimators, the X-ray background that might be produced and scattering cross-sections of the collimator materials.

Vacuum pumps such as Turbo Molecular Pump, Rotary Vane Pump, Ion Getter Pump, and Oil Diffusion Pumps were used in the beamline to control vacuum levels.

Various photon detectors were calibrated to select one with the best energy resolution for the use in this facility. A HPGe detector was found to be suitable with a better resolution as compared to Ge (Li) and Si (Li) detectors.

After completion of the construction phase of this work, the beam facility was tested using a proton beam from the AEC Van de Graaff accelerator. The system resolution was investigated using different combinations of collimators. This required proper alignment of these collimators.

To find the resolution of the beam, a Molybdenum wire was scanned across the beam and the emitted X-rays were counted. Beam profiles were produced by plotting X-ray counts against wire positions. The resolution of the beam was taken as Full Width Half Maximum (FWHM) of the profile. The best resolution for this

facility was 90μm.

Development of a Micro-PIXE Facility For analysis of geological Samples

By

P.T.Mkhabela

BSc (Ed) University of North West

(1998)

Dissertation Submitted in Partial Fulfilment

of the Requirements for the Degree of

Master of Science

(Applied Radiation Science and Technology)

University of North West
July 2001

ACKNOWLEDGEMENTS

The most important acknowledgement is to The Council for Nuclear Safety for offering financial support through my studies and The Atomic Energy Corporation that provided the facility to carry out the project. I acknowledge the assistance of Dr CB Franklyn for supervision this work.

TABLE OF CONTENTS

List of tables.

Table of figures

List of Symbols

σ^I = ionization cross-section (barns)

E_0 = the initial ion energy (MeV)

$\sigma^X_p(E)$ = the X-ray production cross-section for a peak k(barns)

S(E) = stopping power for the ion (MeV/cm)

μ = Mass attenuation coefficient (cm^{-1})

C = the relative concentration of the element that produced the peak p

W = atomic weight of the element (g)

N_0 = Avogadro's number

Ω = Solid angle subtended by the detector (sterads)

Q = the total charge hitting the target(C)

ε = Detector efficiency

e = ion charge (Coulomb)

θ_i = the angle of the incoming beam with respect to the target surface normal.

θ_0 = the angle of the outgoing X-ray with respect to the target surface normal.

ω_K = fluorescence yield

n = the principal quantum number

l= the angular momentum quantum number

j = electron spin

Y_p = yield of X-rays (number of X-rays/number of protons)

T = Kinetic energy (MeV)

E_x = the energy of the X-ray (keV)

E_i = the energy corresponding to channel number C_i

ρ = Density of the material (g/cm^3)

CHAPTER 1: INTRODUCTION TO THE STUDY

1.1. Microprobe Beams

Zirkle and Bloom using a Van de Graaff accelerator [LEG97] developed the first collimated microprobe at the University of Chicago in 1953. The first attempts to use a collimated beam for analysis were announced simultaneously by Pierce et al [PIE66] at Harwell and Mak [MAK66] at Lucas Heights as indicated in Table 1.1. Some groups required brighter beams (higher beam current for the same beam size) and it was suggested that the beam from a collimator be focussed strongly by quadrupole lenses. According to Legge [LEG97], the use of quadrupole lenses was started in St. Petersburg by Alexander Dymnikov. He studied positive and negative demagnifying modes of a lens system that was designed by him. Later this lens was called "The Russian Quadruplet".

John Cookson and Frank Pilling had their first focussed microprobe beam operating in 1968. They used the focussing system of four magnetic quadrupoles (the Russian Quadruplet) with 76mm bore on a single-ended Van de Graaff accelerator. This microprobe was developed into a scanning microprobe with a beam spot diameter of a few microns. This was named the ion microprobe and later the name changed to nuclear microprobe since this system was used for nuclear analytical techniques.

In 1972, Kurt Traxel reduced scattering by polishing slits and introduced new

collimator designs [TRA95]. All causes of collimator scattering were studied by Nobilling et al [NOB75].

Table 1.1 Collimated Microprobes [CAH80]

Year	Laboratory	Ion,* energy(MeV)	Minimum spot size(μm)
1966	Harwell	P, 1.8	660
1966	Lucas Heights	P, 0.9	100
1971	Los Alamos	P, 4.0	30
1973	Munich	α, 1.5	10
1975	Heidelberg	P, 1.0	1
1975	MIT	P, 2.5	25
1976	Florida State	P, 4.7	30
1978	Brookhaven	P, 3.5	25
1978	Grumman	D, 1.6	12

*P =proton, α =^{4}He particle, D =deuteron

1.2. PIXE

Particle-Induced X-ray Emission (PIXE) was first introduced at Lund Institute of Technology in 1970 following the advent of Lithium drifted Silicon Detectors [Si (Li)] which were sufficiently sensitive to X-rays of energy 2-100keV in the late 1960's. It involves the excitation of atoms by irradiating samples with an energetic proton beam produced from a Van de Graaff accelerator. X-rays generated from samples are

collected by a Si (Li) detector and sorted according to their energies and counted. A spectrum of X-rays is produced and analysed for identification and quantification of elements. Most elements above Na (Z=11) can be analysed in the X-ray energy spectrum by using solid state detectors. This range can be extended down to Beryllium with the use of crystal spectrometers or windowless semiconductor detectors [COH89].

CHAPTER 2: THEORETICAL BACKGROUND

2.1. X-ray Transitions

According to quantum mechanics electrons occupy stable state energy levels such as shown in Figure 2.1. The configurations of these electrons in different atoms are similar, but the energy levels are different. When fast charged particles such as protons or alphas or any form of energy such as photons approach the atom within a short distance to the outer electron orbitals, they may knock out the K- and L- shell electrons creating vacancies. When outer electrons fill these vacancies during reorganisation of the bound electrons, the excess energy is carried away by electrons from inner shells (Auger electrons) or photons in the form of X-rays as illustrated in Figure 2.2. The emitted X-rays are characteristic of the elements from which they originate.

For the X-rays to be emitted, the electronic transition must be allowed based on conservation principles. All allowable transitions have $\Delta n>0$; $\Delta l=\pm 1$; and $\Delta j=0, \pm 1$.

Where n =the principal quantum number

l =orbital angular momentum

j =electron spin number.

Transitions not having these values occur with very low probability and are called forbidden transitions. The K- and L-series transitions have been studied by

Beulich[BEU]

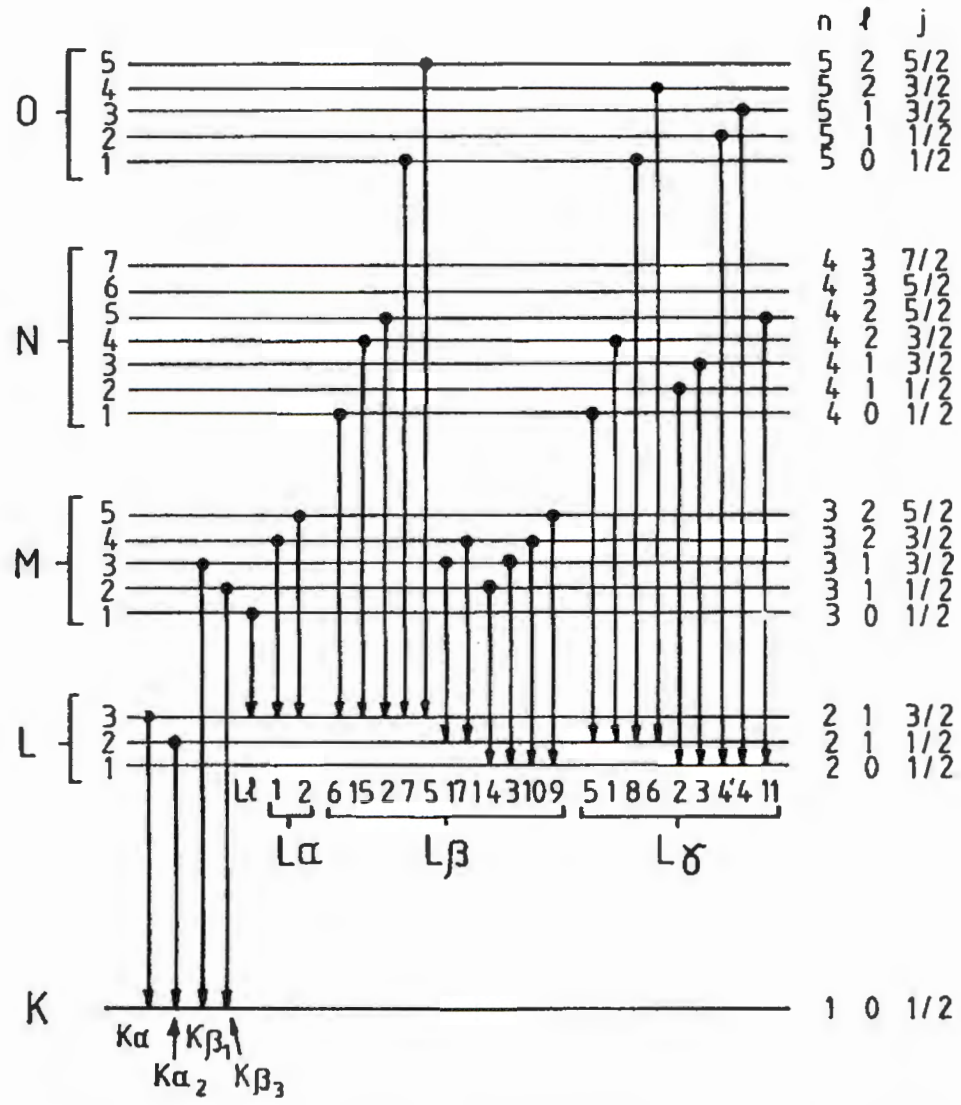

Fig. 2.1 Energy level diagram (not to scale), conventional (Siegbahn) notation on the left and spectroscopic notation on the right. Transitions giving rise to *K* and *L* series lines only are indicated. (from COH89)

2.2. X-ray Production Cross-sections and X-ray Yields

There are many different parameters required for the prediction of X-ray yields [COH87]. These include fluorescence yields and radiative widths [COH81], mass

attenuation coefficients [THI79], ion stopping powers [ZIE85], and X-ray cross-sections.

Several theories exist for the prediction of ionisation cross-sections σ^I. The plane wave Born Approximation Theory was modified by Brandt and Lapicki in 1979 and 1981 respectively. They incorporated polarisation and binding effects in the Perturbed Stationary States (PSS) approximation theory and by correcting for relativistic (R), energy loss (E) and the Coulomb deflection (C) effects. This is generally referred to as the ECPSSR Theory. The ECPSSR theory can be used to calculate ionisation cross-sections σ^I_s for a given shell s = K, L, M... Experiments generally measure the yields Y_p in a given peak p which originate from an X-ray transition filling the vacancy in the shell s. The yields and cross-sections are related in the following manner:

$$Y_p = \frac{CN_0\Omega Q\varepsilon}{4\pi We}\int_{E_0}^{0}\sigma_p^x(E)\exp[-\mu x]\frac{dE}{S(E)}$$

Where

$$\mu x = \mu\int_{E_0}^{E}\frac{\cos(\theta_i)}{\cos(\theta_0)}\frac{dE}{S(E)}$$

For instance, the K-shell X-ray production cross-sections σ^X_p for a peak p and the ionisation cross-section σ^I_s are related as follows:

$$\sigma_{Kp}^x = \omega_K\sigma_K^I$$

Where ω_K =the K-shell fluorescence yield.

Figure 2.2: X-ray emission principle

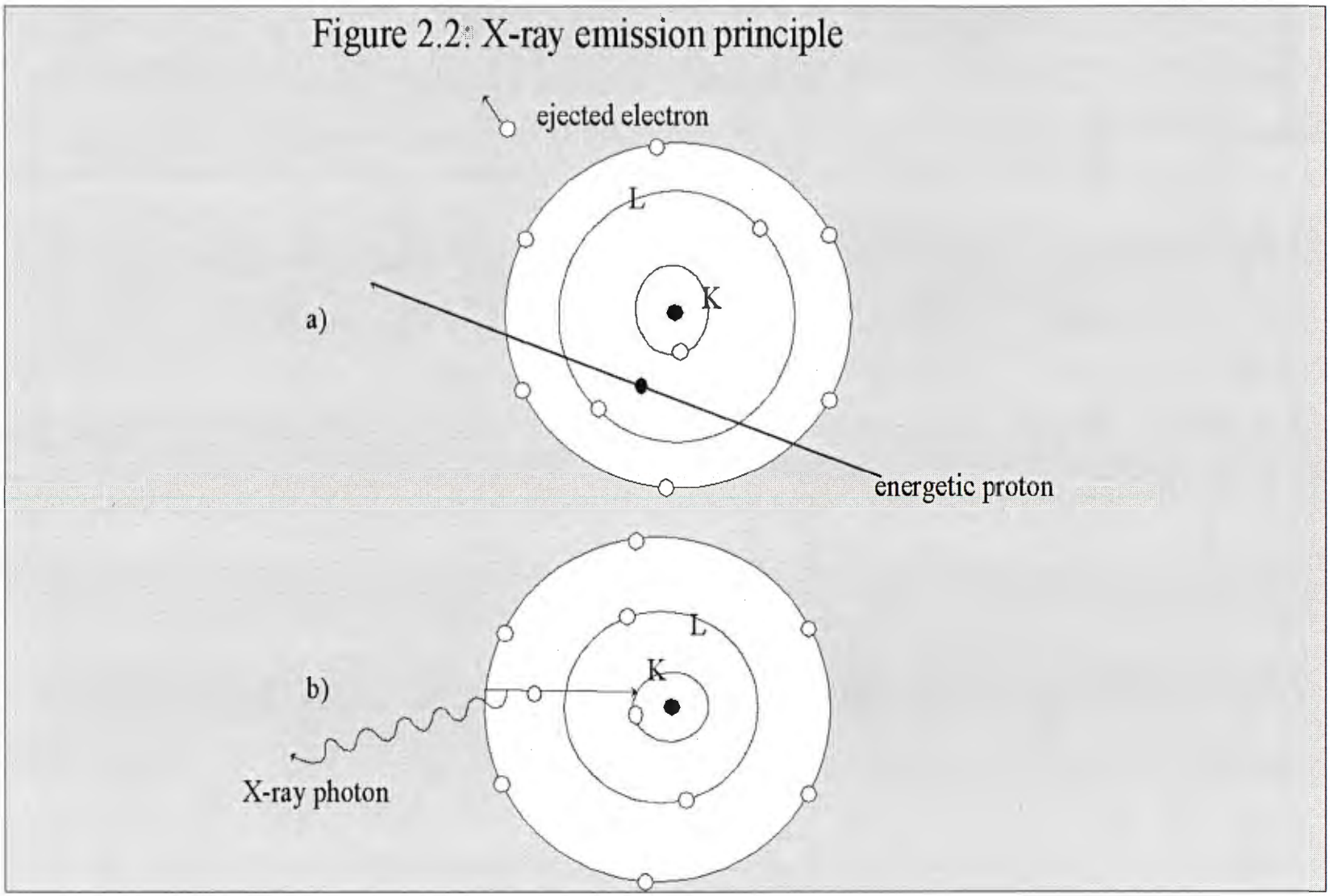

As the proton energy is increased the agreement between theory and experiment improves. However, at low proton energies, there is slight disagreement between the ECPSSR theory and experiment. Figure 2.3. illustrates how the X-ray ionization cross-section varies as the energy of the incident particle is increased. In general, the ionisation cross-section increases as the ion energy increases.

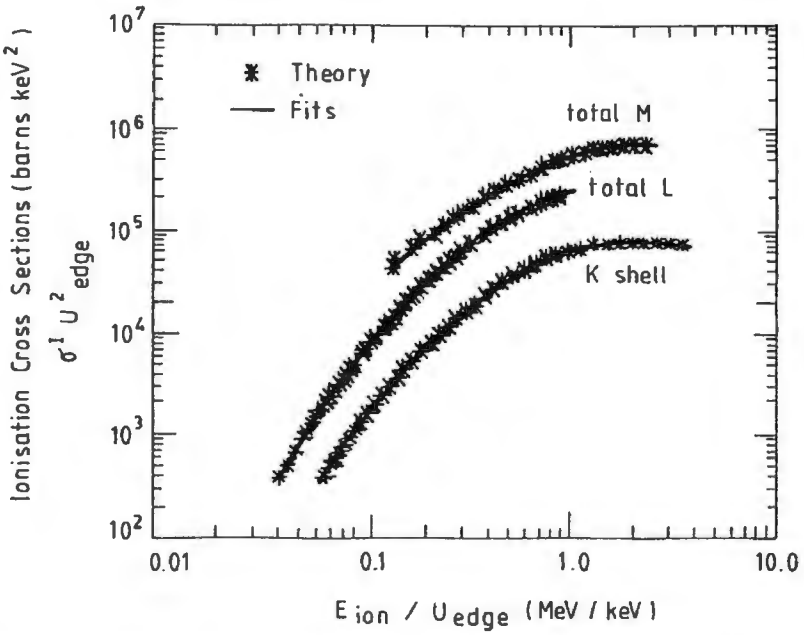

Fig. 2.3 The *K*, *L* (ECPSSR) and *M* (CPWBA) ionisation cross-sections as a function of the ion *E/U* for proton bombardment. *U* (keV) is the target atom absorption edge energy. The points represent the theory and the solid line the polynomial fits described in the text.

The X-ray yield increases by more than an order of magnitude when the proton energy increases from 1 to 4 MeV as illustrated in Figure 2.4, and naturally depend on atomic number Z_2 (target material). The increase in yield for Z_2 between 11 and 92 is one of the major advantages of the PIXE technique and results in very high data acquisition in this range.

Figure 2.4: X-ray Yields as a function of Atomic Number

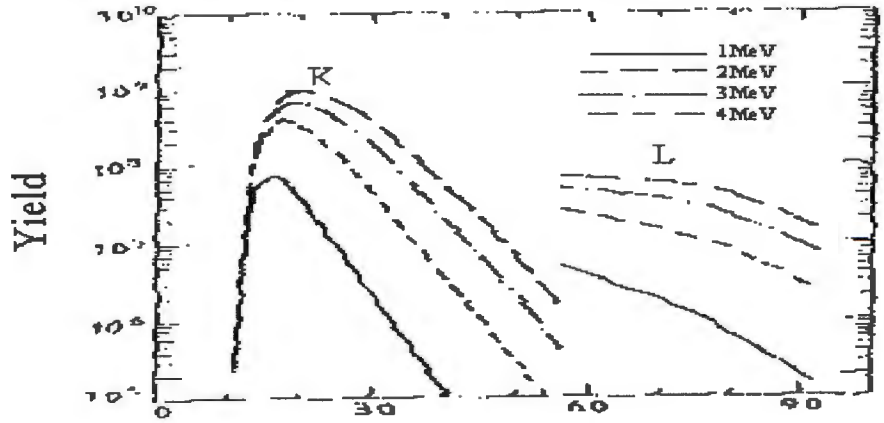

In Figure 2.4 the K_α yields become small for Z_2 =30, at approximately 50 L_α yields start to dominate and reasonable sensitivity is obtained over a large fraction of the periodic table. The detection efficiency near the region Z_2= 12 is very low and decreasing for lower X-ray energies resulting in a drop in yield. The low ionisation cross-sections above Z_2=80 results in low L_α yields and low K_α yield in above Z_2= 30, but the M-shell X-rays take over.

The maximum ionisation cross-section occurs around ion energy of

$$E = \frac{134U^2 s^4}{Z_2^2} \left(MeV/amu \right)$$

Where U =electron binding energy of target electrons in the shell s. This is called the velocity-matching peak and occurs when ions and target shell electrons have similar velocities. For phosphorus (U=2.103keV, Z_2=15) and Calcium (U=3.691keV, Z_2=20).

This corresponds to 2.4 and 4.6MeV/amu respectively. This is one of the reasons why the choice of energies for the PIXE technique lies between 2 and 4MeV/amu.

2.3. Spectrum Analysis

Quantitative PIXE analysis involves measuring the intensity of characteristic X-rays emitted from the sample and converting this information into concentration data. The analysis is often complicated by the presence of background radiation and escape peaks that are superimposed on the spectra. These form additional limiting factors in the sensitivity of the PIXE technique.

2.3.1. Background Radiation

2.3.1.1. Secondary Electron Bremsstrahlung

This is low energy background due to bremsstrahlung of secondary electrons ejected from target atoms during irradiation. The maximum energy (T) of the secondary electron is

$$T = \frac{4mM_1E_1}{(m+M_1)^2}$$

$$T \sim \frac{4mE_1}{M_1}$$

Where m =the electron mass

M_1 =the ion mass

E_1 =ion energy

For 2.4MeV protons T~4.8keV, the highest Secondary Electron Bremsstrahlung energy.

2.3.1.2. Projectile Bremsstrahlung

Ions decelerating in the target atoms will also produce bremsstrahlung. This is a strong function of ion mass and since M_1 is several orders of magnitude of m, the ion bremsstrahlung is much less than electron bremsstrahlung.

2.3.1.3. Compton Scattering

Elements with high cross-sections for (ion, γ) reactions produce γ-rays which Compton scatter in the x-ray detector producing an additional high-energy X-ray background.

2.3.2. Escape peaks

There is a probability that an X-ray of energy E_x will interact with the semiconductor atoms in the detector and produce a K X-ray if it has sufficient energy. This X-ray may then completely escape from the detector volume. In this way it is lost from the full energy peak and the residual energy appears in the spectrum as a separate peak. For Si this peak has energy of

$E = E_x - 1.74keV$

The ratio of the intensity of the escape peak to the parent peak (f_{esc}) can be fitted empirically as a function of X-ray energy:

$$\ln(f_{esc}) = -3.0183 - 0.51995E_x + 0.01344E_x^2$$

where E_x is in keV. These peaks are small but should be included to prevent errors in element identification and to improve the limit of detection.

2.4. Equipment for PIXE

There are different types of equipment required for the establishment of a PIXE system. An accelerator is of prime importance for a PIXE system. Other components include the collimators, vacuum pumps, and focussing magnets as illustrated in Figure 2.11.

Figure 2.12: Equipment for micro-PIXE Beamline

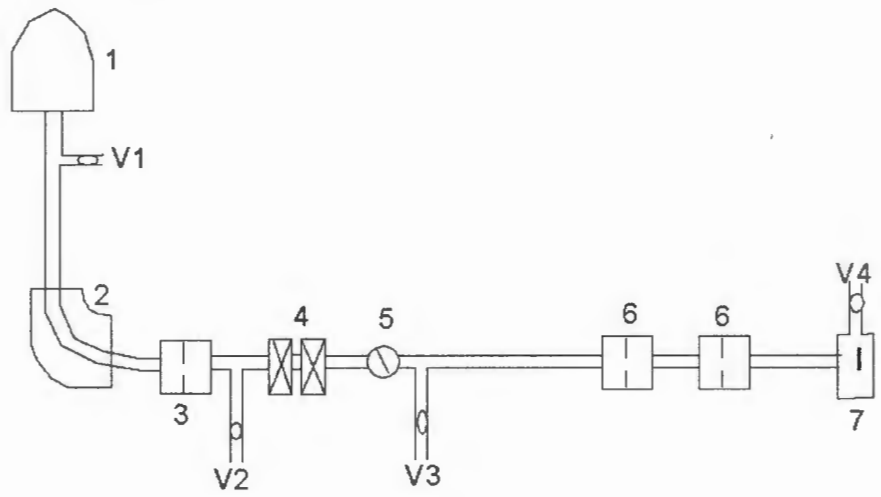

1. 3.7 MeV Van de Graaff accelerator
2. Bending Magnet
3. Control Slits
4. Quadrupole Magnets
5. Viewer
6. Defining Collimators

V1=Turbo Pump
V2=Diffusion Pump
V3=Getter Ion Pump
V4=Turbo Pump

2.4.1. Accelerator

The process of proton-acceleration is started by allowing Hydrogen (H_2) gas to enter a source bottle. The source bottle is made of Pyrex glass. At the top of the bottle is a Tungsten wire that is sealed into the glass and is connected to a 5kV supply.

The protons are created inside the ion source by plasma formation. Wrapped around the glass bottle are two metal bands, at the top and bottom. These bands are connected to a RF (Radio Frequency) source of about 27 MHz. The RF deposits energy into the H_2 molecules until they dissociate into H^+, H_2^+, H_3^+ ions and thus creates the plasma. There are four cylindrical permanent magnets mounted around the bottle to maintain the plasma within the inside of the bottle without hitting the walls.

A voltage is applied between the tungsten wire and the bottom of the source bottle. Once the voltage is applied, protons exit the source bottle and enter the accelerating tube through to the 90^0 analysing magnet. The analysing magnet's function is to guarantee that a single component beam (i.e. a beam of protons with the same kinetic energy) goes to the target chamber. By setting the analysing magnet to the proper field strength the beam component with the correct charge to mass ratio (e/m) will be bent around the magnet and allowed to reach the target.

2.4.2. Vacuum System

The beam handling system is maintained under high vacuum levels by using different types of vacuum pumps. The vacuum pumps that are available include turbo molecular pumps(TM), oil diffusion pumps (OD), rotary vane pumps (RV), and ion getter pumps (GI). These pumps operate at different vacuum levels as shown in Table 2.1.

Table 2.1 Levels of operation of different vacuum pumps

Vacuum Range	Pressure (Pa)	Type of Pump
Coarse Vacuum	10^{5}-10^{2}	Rotary Vane
Medium High Vacuum	10^{2}-10^{-1}	Rotary Vane
High Vacuum	10^{-1}-10^{-5}	Diffusion and Turbo Molecular
Ultra High Vacuum	10^{-5}-10^{-6} and below	Ion Getter

2.4.2.1. Oil Diffusion Pump

Figure 2.5(a) shows a schematic representation of an oil diffusion pump. The vapour stream expelled from the jets at supersonic speed carries the diffused-in gas molecules to the cooled pump wall. There the oil condenses and flows back to the boiler section as a thin film. The pumped gases are thereby released and cannot diffuse back towards the high vacuum side against the vapour stream. Thus the oil

continuously purifies itself. In this way the gases are compressed in three or four stages, depending on the pump, and removed by a roughing pump such as the Rotary Vane into the atmosphere.

Figure 2.5(a) Oil Diffusion Pump

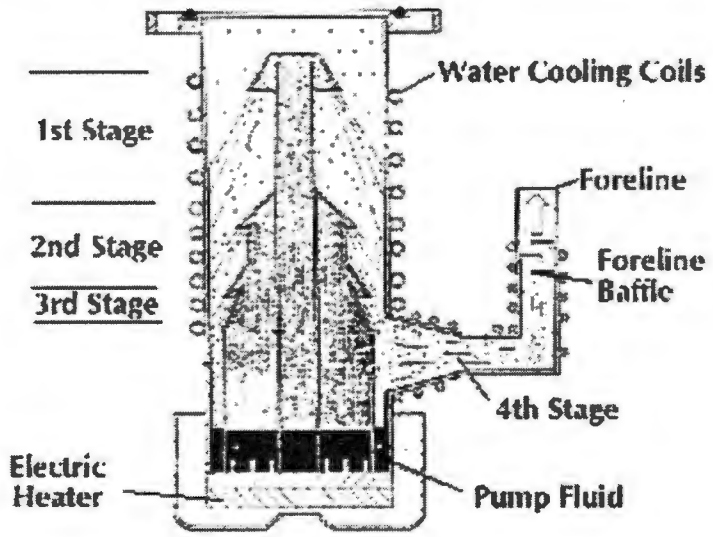

2.4.2.2. Turbo Molecular Pump

The turbo molecular pump mainly comprises a rotor and a stator as shown in Figure 2.5(b). Rotating and stationary discs are arranged alternatingly. All discs are fitted with inclined, coiled channels with the channels of the rotor discs fitted inversely to the stator discs.

Figure 2.5(b): Turbo Molecular Pump

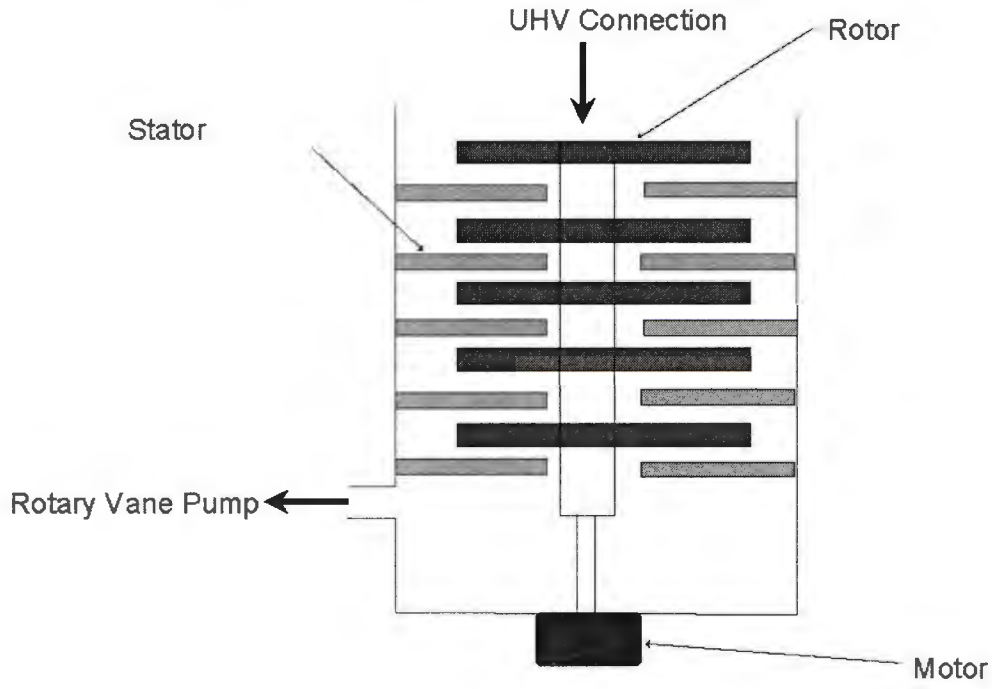

Each of these discs is an elementary molecular pump. All the channels of the discs are connected in parallel. One rotor disc combined with one stator disc form a pumping stage. Thus a turbo molecular pump consists of several pumping stages connected in series, these stages in turn created by a series of elementary molecular pumps being connected in parallel.

2.4.2.3. Rotary Vane Pump

Figure 2.5(c)Rotary Vane Pump

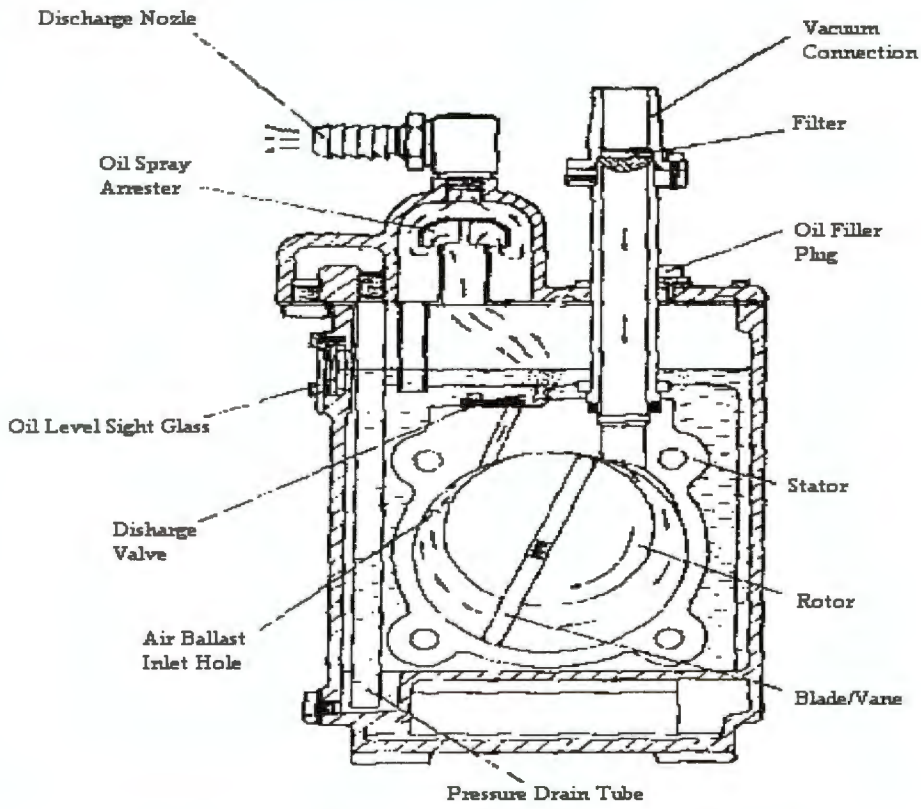

The pump operates on a rotary vane principle (see Figure 2.5(c)). A rotor mounted on an eccentric shaft rotates within a cylindrical stator forming a working chamber in a sickle-shaped cross-section. The working chamber is divided into two chambers of varying volume by means of two vanes moving in rotor slots. The pressure chamber is enlarged when the vanes rotate from the vertical position. The upper vane separates the exhaust from the intake channel. The gas in the pressure chamber is compressed and after reaching atmospheric pressure, it is expelled via the pump

valve.

2.4.2.4. Ion Getter Pump

Figure 2.5(d): Ion Getter Pump

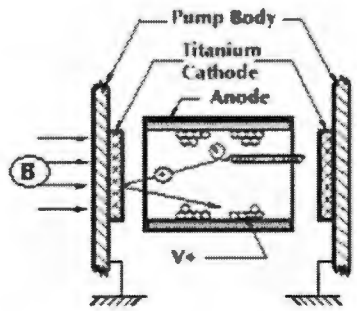

The basic principle of this pump is the sorption of gas by a reactive metal in the presence of an ionising electric field. This is known as gettering. Many materials such as magnesium, calcium, barium and mixtures of various reactive metals that readily form low-pressure oxides and nitrides have been used [SPI63]. Titanium is evaporated by heating through electron bombardment and continuously pumped to improve the system for short periods.

A discharge is created between a hot hollow electron source and a cold hollow cathode reflector. The electrons emitted by the hot cathode are trapped by an axial magnetic field and ionise the gas in the pump. The ionised gas molecules travel to one of the cathodes where they strike some surface and become de-ionised then pumped away by a rotary vane pump.

2.4.3. Quadrupole Magnets

A plasma lens focuses ion beams in the same way that an optical lens focuses light. Magnetic fields can be used to focus or redirect the path of charged particles. Quadrupole magnets may therefore constitute a lens system for a PIXE beamline arrangement. A quadrupole lens consists of four magnets aligned as shown in Figure 2.6 which also shows the directions of magnetic field and field force that would be exerted on positively charged particles entering this system (towards the reader) perpendicular to this page.

Figure 2.6: Quadrupole Magnetic Lens Showing magnetic field direction (a), and magnetic force directions(b). The ultimate effect is focussing in one plane an d defocussing in the other.

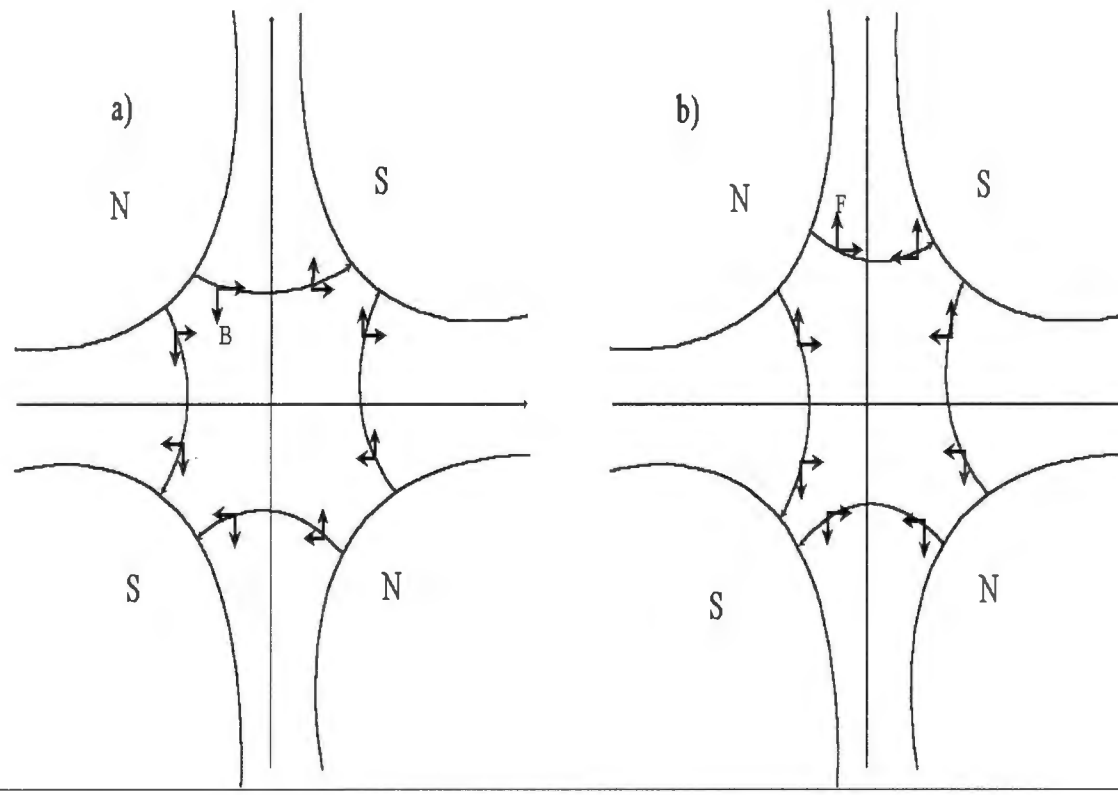

As a beam of charged particles passes through the centre of this lens it is focussed horizontally and defocused vertically (or vice versa) depending on the magnetic configuration and the charge of the particles. The trajectories of these particles can be determined using various computer codes [LEE93, MEO94].

A variety of combinations of quadrupole magnets can be employed as doublets, triplets and quadruplets for the lens system. The principal planes may coincide, be close together, be apart or be outside the elements comprising the system. An example of the latter is a quadrupole pair. For a quadrupole pair, the principal planes are displaced towards and usually, beyond the focusing element of the pair. The magnification between the object and the image planes is M= q/p

Since the quadrupole is different in the two planes (x and y), both situations must be examined. Typically for a quadrupole pair, the ratio M_y/M_x = 20:1. This is the first-order distortion [BRO70]. For instance, if a source in Figure 2.11 is a circular spot at A, the image at B will appear as a long line. P1 and P2 are principal planes, p is the object distance, and q is the image distance.

Most facilities use doublets and quadruplets since it has an advantage of symmetry as compared to the other combinations. This arrangement may require the use of position alignment on an optical bench to obtain optimum focusing of particles.

Figure 2.11: Optics of a Quadrupole Pair

in one plane

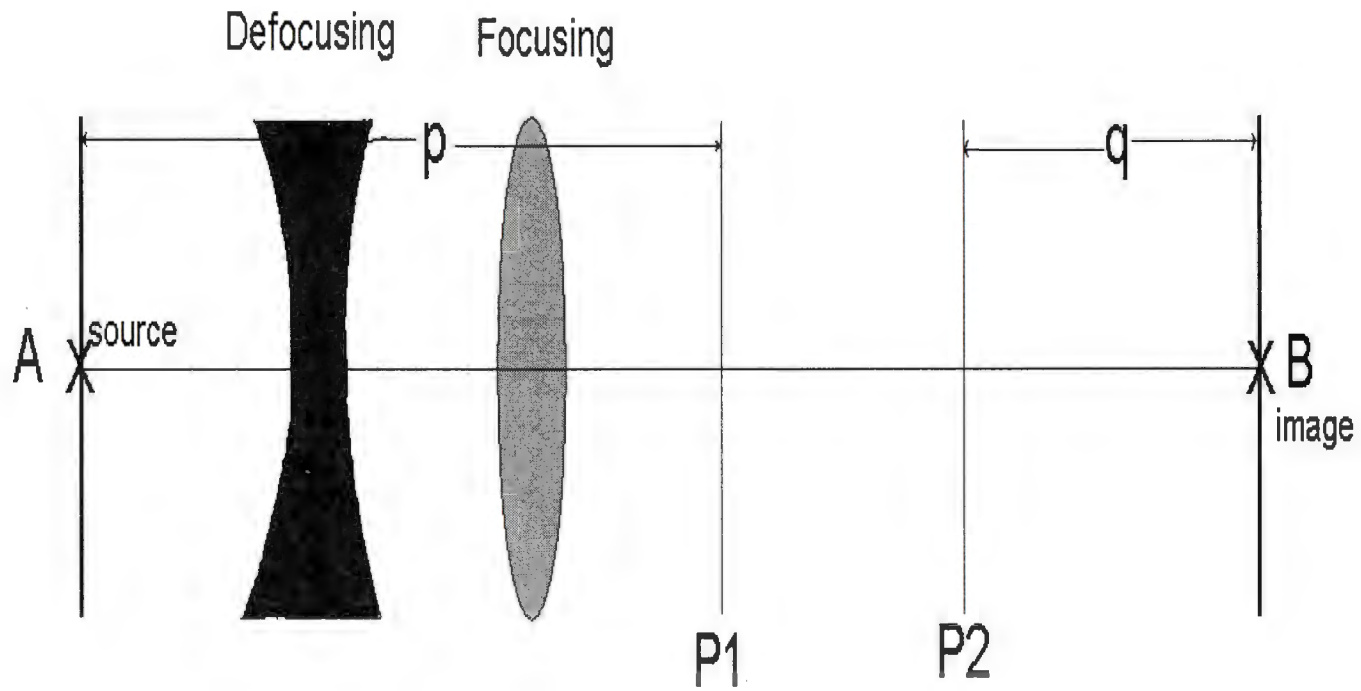

2.4.4. Collimators

Figure 2.7: Collimator slit designs investigated by Al-Ghazi [ALG82]

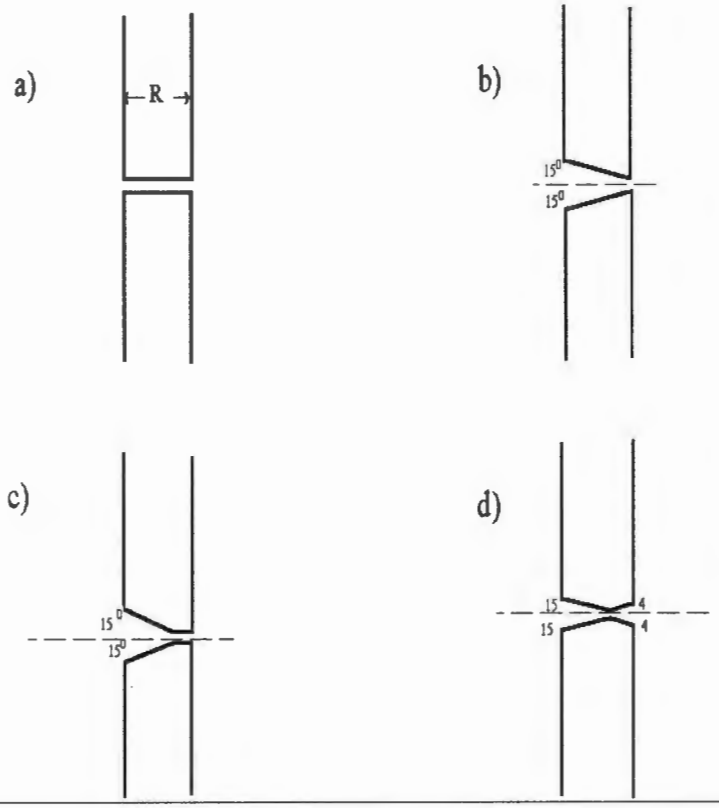

The choice of collimator material is crucial in the set-up of micro-beams. Tantalum and graphite have low cross-section for (ion, γ) reactions hence are generally used for defining apertures in order to minimise the γ-and X-ray background.

The designs of these collimators need to be taken into consideration because some designs produce an excessive amount of scattering. Collimator slit designs investigated by Al-Ghazi et al [ALG82] are shown in Figure 2.7. Burge and Smith [BUR62] did a detailed study of slit scattering. They concluded that the amount of slit

scattering for different collimator material is roughly proportional to $A/(\rho Z^{1/2})$ Where A is the atomic weight, Z is atomic number of slit material and ρ the density. This favours elements such as Tantalum and Nickel.

2.4.5. Measurement of Beam Charge

With a very thin specimen, the beam can pass though the specimen and be collected in a Faraday cage, integrated and digitised on the beamstop. As the specimen becomes thicker, the beam undergoes scattering and some protons may be stopped at the back wall of the target chamber. A current digitizer can be used to integrate the number of protons incident on the target and its accuracy is checked by a high impedance (R_i=1000MΩ) voltmeter [MAL82].

Secondary electrons may also reach the beam stop and cause erroneous readings of proton charge. These problems are resolved by coupling the chamber and the downstream beam-line electrically to act as a single Faraday cup, isolated from the beamline upstream. Secondary electrons are produced when the protons strike the target and some of those produced near the surface of the material, are emitted from the sample. The relative yield of such electrons depends on the proton energy and sample surface composition [THO77]. The charge of these electrons has to be measured for accurate charge integration. To avoid the escape of the electrons through the last collimator, a negatively biased electron suppressor is inserted between it and the sample.

2.4.6. Detectors

A typical detector element is a single crystal of Germanium or Silicon made into a diode to withstand high bias voltage at cryogenic temperatures. Electron-hole pairs produced by absorption of an X-ray or gamma ray photon are swept to opposite contacts by an electric field. A charge sensitive preamplifier integrates the resulting current pulse, producing an output voltage pulse with height proportional to the incident photon energy. The amplifier provides additional amplification or pulse shaping. Output from the amplifier goes to the Pulse Height Analyser where they are sorted and stored by channel number according to their pulse height.

Within the pulse height analyser, the input signal goes directly to the analog-to-digital converter (ADC). The ADC measures the amplitude of each incoming pulse and converts it into a digital signal proportional to a pulse height. The digital signal goes to the front-end-processor that adds a count to that unique memory address which represents the appropriate pulse height as a channel number. The channel number therefore represents the energy of the incoming photon.

2.4.6.1. Amplifier (Shaping Time, Noise and Pileup)

Shaping time (τ) affects the amount of system noise and the degree of pulse pileup experienced. Typical noise minimum (or noise corner) is

4-8μs for coaxial Ge detectors (GEM, GMX, GLI, and GWL)

6-10μs for planar Ge detectors LEPS (GLP)

10-14μs for planar Si (Li) detectors (SLP).

Pileup at the amplifier output depends strongly on the count rate and the amplifier time constant. The longer the time constant the longer the signal is away from the baseline for a given pulse i.e. the greater the probability that an additional pulse will occur while the signal is away from the baseline due to a previous pulse. The probability of pulse pileup increases with an increase of count rate. The fraction f of the pulses that will be piled-up is

$$f = 1 - e^{-R\tau_d}$$

where R= count rate and τ_d is the dead time associated with each pulse.

2.4.6.2. Detector Dead Time

In all detectors systems, there will be a minimum amount of time that must separate two events in order to record them as two separate pulses. In some cases the limiting time is set by the process in the detector itself and in other cases the limit arises in the electronics. This minimum time is called the dead time of the counting system.

2.4.6.3. Detector resolution

The resolution of the detector is specified by the Full Width at Half Maximum (FWHM) of the detected photon peaks. The resolution of the detectors is normally determined by three factors: the inherent statistical spread in the number of charge carriers, variation in the charge collection efficiency, and contribution from electronic noise. The FWHM W_t of a typical peak in a spectrum due to the detection of a mono-

energetic X- or gamma ray can be written as follows

$$W_t^2 = W_D^2 + W_X^2 + W_e^2$$

W_D represents the inherent statistical fluctuation in the number of charge carriers created.

$$W_D^2 = 2.355^2(FeE)$$

Where, F is the Fano factor (F = 0.11±0.04 for Si and 0.13±0.05 for Ge)

e is the average energy required to form an electron-hole pair (e = 3.81eV for Si and 2.98eV for Ge)

E = photon energy in eV.

W_x is due to incomplete charge collection and is more significant in detectors of large volume and low average electric field. It can be determined experimentally by obtaining a series of FWHM measurements as the applied voltage is varied. A plot of the observed FWHM versus the reciprocal of the average applied voltage within the detector allows the extrapolation to infinite field conditions. The residual FWHM given by this extrapolation is then assumed to arise from the remaining two factors, i.e. W_D and W_e.

W_e represents the broadening effects of all electronic components following the detector. Its magnitude can be determined by supplying output of a precision pulser and recording the peak in the pulse-height spectrum. Thus the resolution variation between detectors arise from the difference in charge collection efficiency, the noise

and in stability of the electronics.

2.4.6.4. Detection Efficiency

The efficiency and physical properties of X-ray detectors have been studied in the past [SHI79, BAR84, CAM84]. For primary charged particles such as alpha and beta particles, interaction in the form of ionisation or excitation will take place immediately upon entry of the particle into the active volume of the detector. Thus it is often easy to arrange a situation in which a detector will see every alpha or beta particle which enters its active volume. The detector is said to have a counting efficiency of 100% under these conditions.

On the other hand neutrons, electromagnetic radiation must first undergo significant interactions in the detector before detection is possible. Hence, detectors are often less than 100% efficient. The efficiency relates the number of pulses counted to the number of photons incident on the detector.

Figure 2.8: Efficiency of Si(Li) Detector[JOH88]

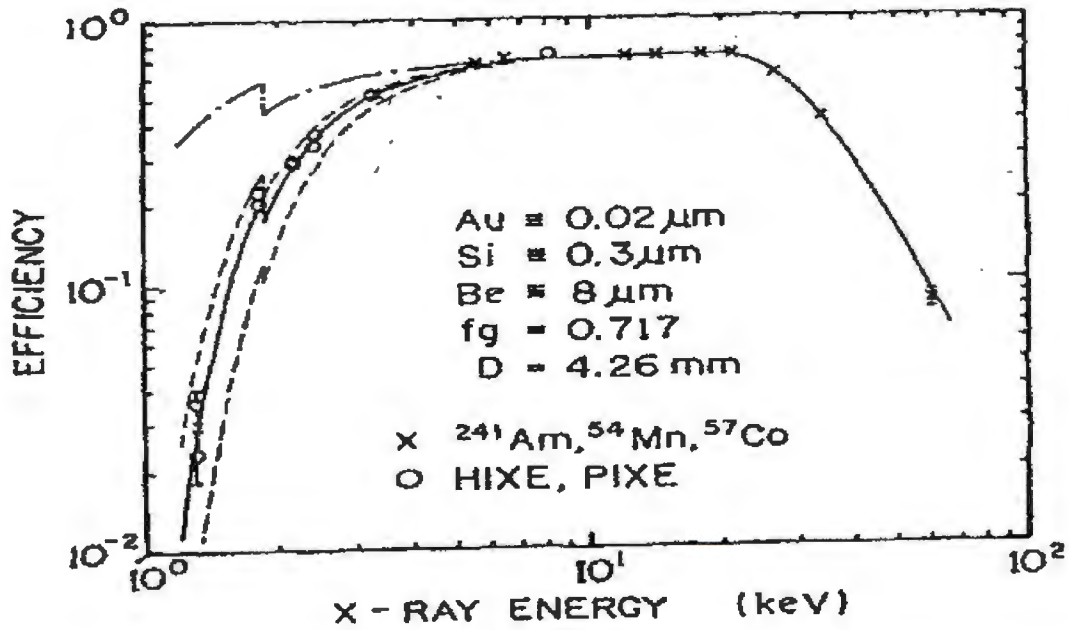

Counting efficiencies are subdivided into two classes: absolute and intrinsic. Absolute efficiency ε_{abs}

$$\varepsilon_{abs} = \frac{N_p}{N_e}$$

where N_p =number of pulses recorded

N_e =number of radiation quanta emitted by source.

ε_{abs} depends on detector properties and the counting geometry (primarily the distance from the source to the detector).

The intrinsic efficiency ε_{int}

$$\varepsilon_{int} = \frac{N_p}{N_i}$$

N_i =number of quanta incident on detector)

For isotropic sources

$$\varepsilon_{\text{int}} = \varepsilon_{abs} * \frac{4\pi}{\Omega}$$

where Ω is the solid angle of the detector seen from the actual source position. ε_{int} depends on the detector material, the radiation energy and the physical thickness of the detector in the direction of the incident radiation. Typical efficiency calibrations for Si(Li) (for X-rays) and Intrinsic Ge (for gamma rays) detectors are shown in Figure 2.8 and 2.9 respectively.

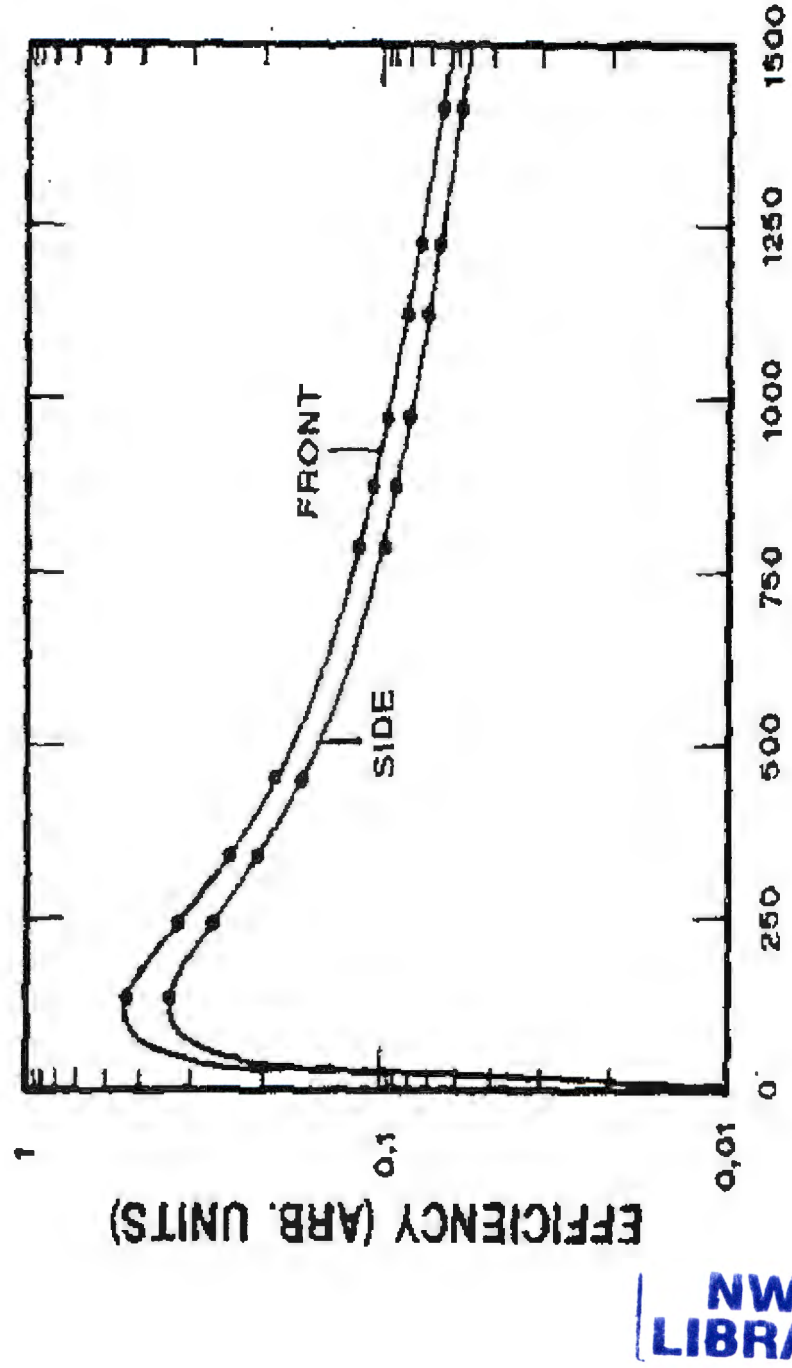

Figure 2.9: Intrinsic Germanium Detector Efficiency [PRO89]

2.4.6.5. Energy Calibration

In gamma and X-ray spectroscopy the pulse height scale must be calibrated so that various peaks can be properly identified. This is achieved by using a source that would provide photons of known energies in the spectrum. Once the energy calibration points have been established over the entire energy range of interest, a calibration curve relating energy to channel number is derived. Common techniques involve the least square fitting of a polynomial of the form

$$E_i = \sum_{n=0}^{N} a_n C_i^n$$

where E_i is the energy corresponding to the channel number C_i.

Polynomials of order N=2 or 3 are normally adequate for typical Ge detectors, depending on the severity of non-linearity that is present.

2.5. Beam Profile Measurement

The intensity of the beam along the two transverse coordinates of the beam is measured and the beam position is derived from this profile measurement. Ideally the beam profile should exhibit a Gaussian distribution in both the x- and y-coordinates where the beam forms the z-axis, but most distributions are distorted as the one shown in Figure 4.5.

2.5.1. Factors Affecting the Beam Profile Measurement

Collimated beams always display a halo due to various factors [WAT95]. For example scattering from collimator slits, the electron suppressor, stray magnetic fields, poor vacuum, oscillating electric fields and vibrations.

2.5.1.1. Slit Scattering

Many collimated beams suffer from scattering at the collimator slits and the intensity of the beam spreads due to slit scattering. About 25% of the beam intensity can be distributed in a halo of several 100 micrometers around the central beam. To solve this problem properly designed and manufactured collimators should be able to suppress slit scattering.

The scattering of protons from the collimator produces a halo around the beam core. Using Tantalum rather than carbon and using an anti-scattering design can reduce this.

2.5.1.2. Mechanical Instability

Mechanical movement of the target is very crucial since the target is susceptible to vibration due to the vacuum pumps. This movement contributes to the problem and causes the beam halo to worsen. Since the target is not mechanically isolated from the vibrations of the vacuum pumps, it is wise to build the system on a heavy concrete base to dampen the vibrations.

2.5.1.3. Stray Magnetic Fields

The effects of stray magnetic fields were investigated at the Singapore facility by Watt et al [WAT95] in 1995. The beam was investigated with magnetic equipment placed at different positions along the beamline. The discussion is based on the fact that beam-lines are inconveniently situated next to other beamlines and respond to AC magnetic fields from vacuum pumps(motors), electronic and electrical instruments (transformers), or electrically activated switches. Hence the magnetic fields in the neighbouring equipment should be investigated

2.6. Advantages of PIXE Technique

Advantages associated with PIXE technique are well documented [JOH86, CAH80, ALG82, JOH92, PAL96]. The experience with the groups that have used PIXE for analytical purposes is summarised below.

The detection limits of PIXE are in the 10^{-12}g range [see Figure 2.10]. With smaller samples the detection limits become correspondingly smaller. A focussed microbeam of a spatial resolution of 1μm the minimum detectable amounts are of the order of 10^{-16}-10^{-17}g.

PIXE is a versatile technique and any solid sample can be directly mounted in the irradiation chamber. If samples do not fit into the chamber, they are irradiated outside

the chamber in air. This is known as external PIXE. However, a possible disadvantage would be the loss of low energy X-rays that can be attenuated by air.

PIXE is a non-destructive technique, but the only damage to the sample may be due to heating and radiation from the beam. This can be avoided by maintaining a low current density and total charge. When the largest solid angle is used, PIXE data can be acquired with low beam currents.

Figure 2.10: Minimum Detectable Concentration (JOH86)

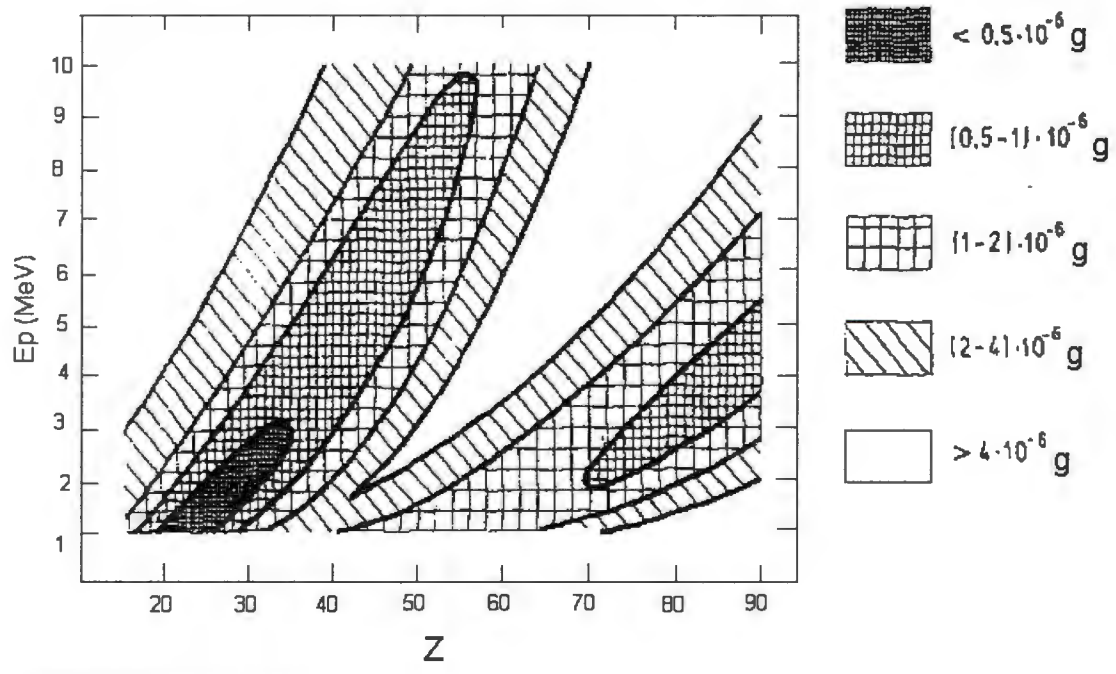

All elements from Silicon to Uranium are detectable with relatively reasonable sensitivity from element to element as illustrated in Figure 2.4. X-rays from elements below Na cannot be seen because they are absorbed in either the detector window or

the atmosphere between the detector and sample. With crystal spectrometers or windowless semiconductor detectors, this range can be extended down to Beryllium [COH89].

The particle beam can be focussed to a very small size to allow sensitive analysis with a good spatial resolution. There is less background radiation from Bremsstrahlung as compared to using electrons as excitation radiation.

2.7. Applications of the micro-PIXE Technique in Geology and Mineralogy

A number of features are essential for geological applications of a proton microprobe.

1. Sample viewing about 100 times magnification is needed to enable viewing of microscopic features of the sample.
2. Micrometer driven stages for positioning the sample accurately are required, preferably computer driven to enable pre-programming of sample co-ordinates.
3. Readily selectable X-ray absorbers are essential to control major element count rate in order to minimise pileup effects and to optimise detection of the elements of interest. Pileup effects can mask lines of interest.

The large effective depth of analysis (20-50 μm) implies that grains greater than 50μm should be selected for analysis to avoid contribution from the substrate overlapping grains. Thus probing with a 10-30 μm beam would be optimal. The validity of the system can be tested against well-known standards.

There are many applications of micro-PIXE in geology and mineralogy [SIE93, PRZ90, SIE91, MAE97]. Micro-PIXE is applied in cosmochemistry, ore mineralogy, and mineral exploration. Most of the geological applications have been carried out with 2-4 MeV proton beams.

2.7.1. Indicator minerals and Diamond exploration

Micro-PIXE is employed to discriminate source rocks, assess diamond prospects, and to study processes affecting diamond formation by using trace element distribution characteristics in minerals like ilmenites and chromites. The actual concentrations of ilmenites precipitating from kimberlites depend on the composition of the parent magma and the crystallisation history. This has implications in the diamond exploration designed to locate kimberlites, the main source of diamonds.

2.7.2. Geothermobarometry

Partitioning of elements between coexisting phases depend sensitively on pressure and temperature. This property is exploited in geothermobarometry for assemblages such as mantle rocks. Electron microprobe can be used to establish various geothermometers using the major and minor elements. Micro-PIXE has been used for the discovery of Ni thermometers for peridotitic garnets, based on the partition between garnet and olivine. With mantle olivine representing a reservoir of Ni, the Ni content in the garnet alone can be used as a thermometer. This is used in the

prospecting of kimberlites and lamproites for likely diamond grades based on garnet concentration alone.

2.7.3. Sulphide mineralogy

Micro-PIXE has been used to determine the trace element distribution in sulphide ore samples with the emphasis on residence of precious metals for beneficiation. For instance, gold occurs as free gold, but in refractory ore it is locked in solid solution or as submicron inclusions in other phases normally relegated to the tailings e.g. pyrite (FeS) and arsenopyrite (FeAsS). Micro-PIXE can determine gold with MDL of 5 ppm in pyrite and 20 ppm in arsenopyrite.

Platinum group elements (PGE: Pt, Pd, Rh, Ru, Os, Ir, and Re) occur mainly as readily separable PGM (Platinum Group Metals) but sulphides often present in the deposit can be significant carriers [PRZ90]. A study of the Merensky Reef ore showed pentlandroite [$(Fe, Ni)_9S_8$] as a significant carrier of Ru, Pd, Rh at levels up to a few hundred ppm and pyrhotite(FeS) as a carrier of Ru(8-12 ppm) with MDL of 2-6 ppm [SIE91]

CHAPTER 3: EXPERIMENTAL PROCEDURES

3.1. Beam Halo Investigation on Old PIXE System

The old PIXE beamline was set-up as shown in Figure 3.1. 3 MeV H^+ ions were produced from the AEC Van de Graaff accelerator with a charge of ~0.12 μC delivered at the target. An intrinsic germanium detector was used for the detection of X-rays emitted from the target materials. The FWHM resolution of the detector was approximately 180 eV at 5.896keV.

The properties of a collimated beam were investigated at a distance of 5 cm from the second collimator. The vacuum was maintained at 6×10^{-6} Torr (~10^{-4}Pa) by a Turbo pump.

A beam profile was performed using about 200 μm diameter NiCr wire. Later a scan was done with the wire placed on an epoxy mount, and smearing was investigated on a polished geological sample.

A program used for data acquisition was EMCAPLUS. Area counts for X-ray peaks of sample materials were plotted against position of the sample (see Figure 4.1). The counts were expressed as percentage of maximum counts for each case.

Figure 3.1: Old PIXE Set-up

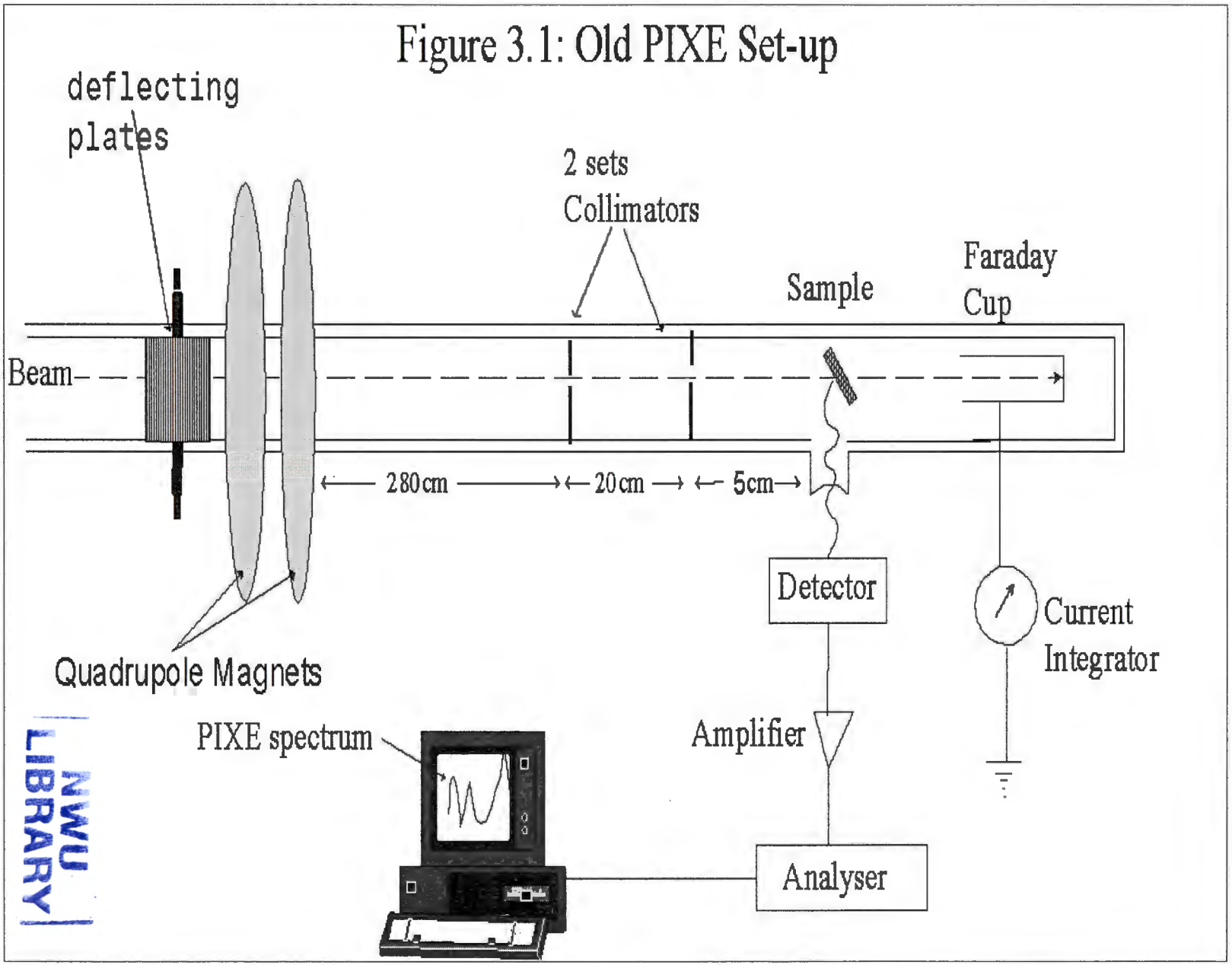

3.2. New PIXE Beamline Set-up

The new PIXE system was set-up as shown in Figure 3.2. The first collimator set was 360cm from the lens system. This was made longer than in the old set-up. Another collimator set was inserted in the chamber to improve the collimation of the beam and minimise the halo effect on the beam. The target holder was mounted at 90 degrees to the beam direction. The beam handling system was set-up as illustrated by Figure 3.5. The aim was to minimise the area that the beam sees on the target. In the old set-up the sample was mounted at 45 degrees to the beam direction. The mounting of the detector was also changed from 90 to 45 degrees with respect to the beam direction in the new system.

The chamber serves as the faraday cup for the new system. A current integrator is connected to the chamber to read the beam current.

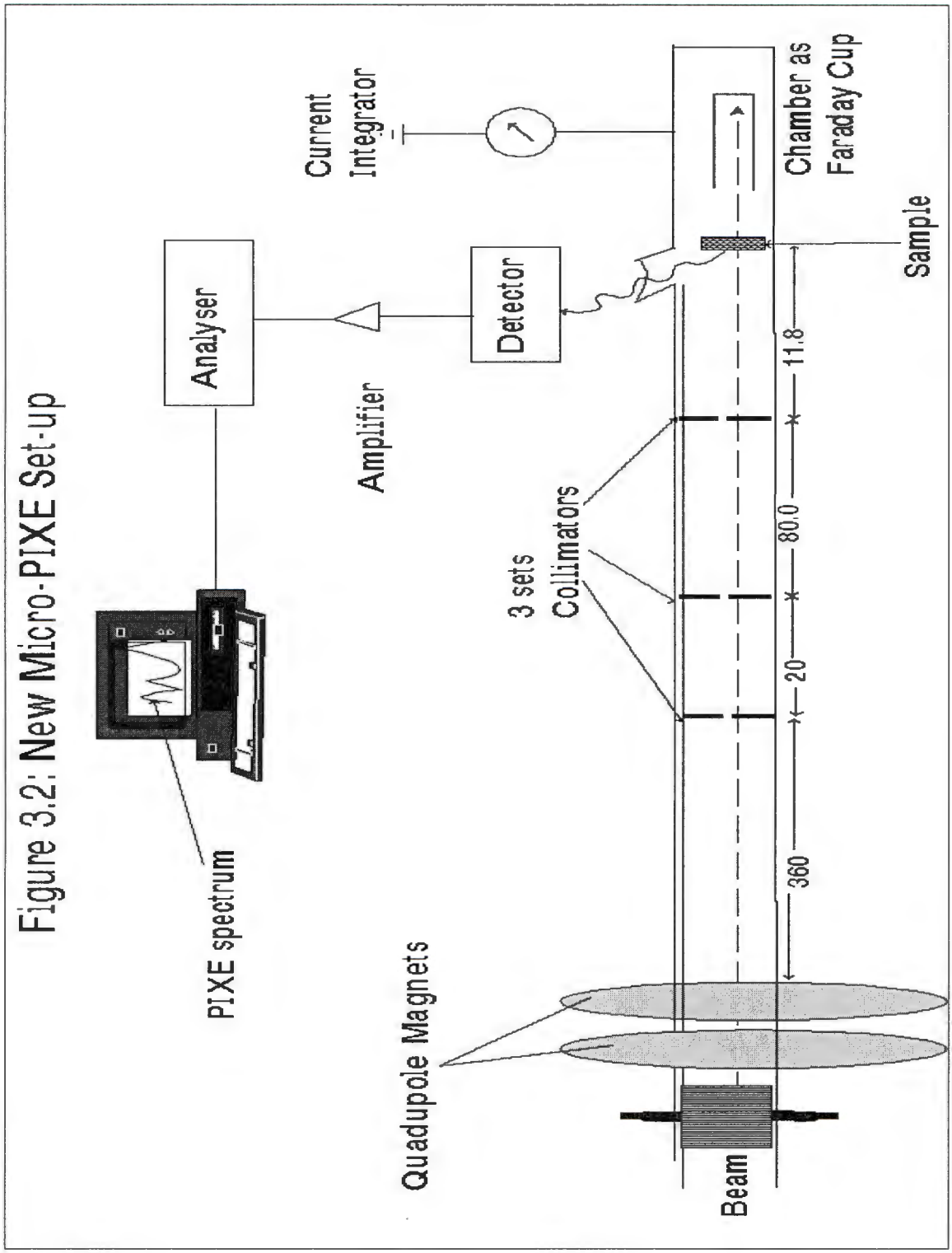

Figure 3.2: New Micro-PIXE Set-up

3.3. Vacuum Pumps

Various vacuum pumps were tested for the use in the new beamline set-up. The

testing of these pumps was conducted as described below:-

3.3.1. Getter Ion Pump

The getter ion pump was connected directly to the beamline. The beamline was pumped down to about 10^{-2} Pa. The ion pump was switched on and water was opened for the cooling system of the pump. The current was about 40 mA and the Voltage 4 kV on the operating unit of the ion pump.

3.3.2. Diffusion Pump

A vacuum system was set-up as shown in figure (Figure 3.6). The rotary vane pump was switched on and V1 was opened. When the vacuum level reached ~8 Pa valve1 was closed and V2 opened. The diffusion pump was switched on and V3 was opened. Vacuum levels were recorded and plotted against time as depicted on Figure 4.3.

Figure 3.6: Setup for testing the Oil Diffusion Pump

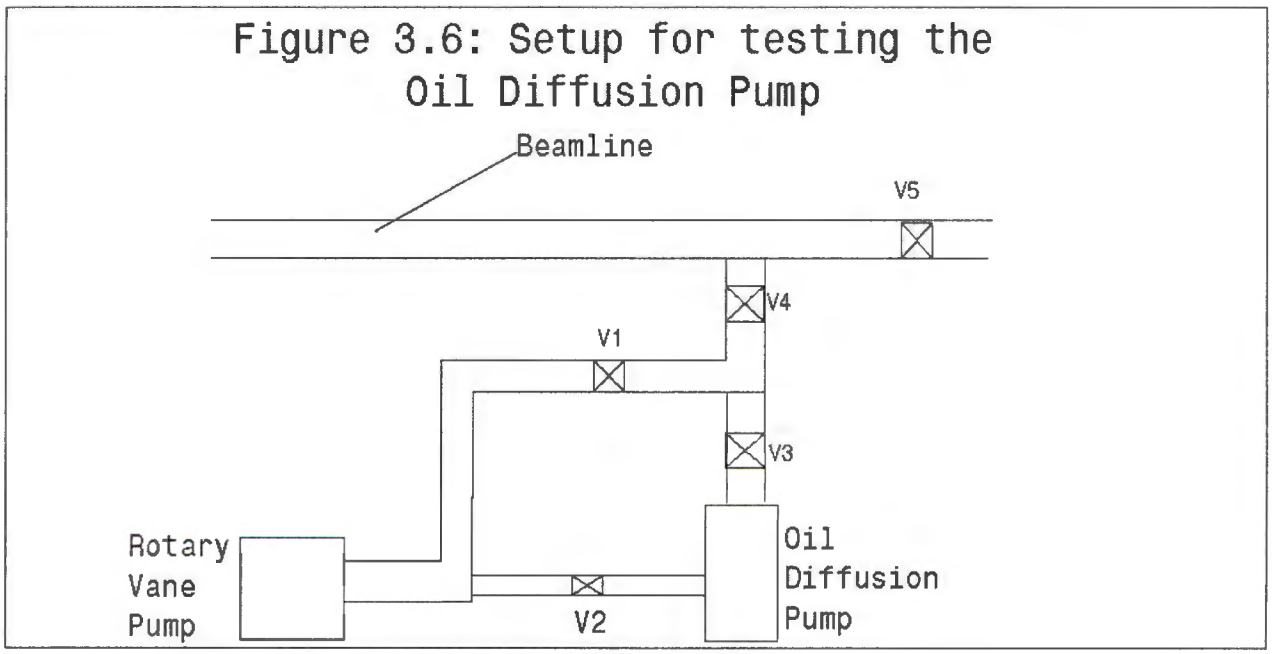

3.3.3. Combination of OD, RV, and TM pumps.

To test the performance of the combination of different pumps, a vacuum system was set-up as shown in Figure 3.7. P1 and P2 were switched on with all the valves closed. To measure low vacuum between V1 and V2, V1 was opened when the pressure was about 0.015mbar on G1. V2 was opened and Turbo pump (P3) and rotary pump (P4) were switched on. The turbo pump was allowed to run until sufficient speed was attained (when the dial was on the green scale). V3 was opened and when G2 read 10^{-1}Pa V4 was opened to evacuate the beamline. The pressure levels were recorded from time to time. Pressure was plotted against time (see Figure 4.4).

Figure 3.7:Setup for testing combined Pumps

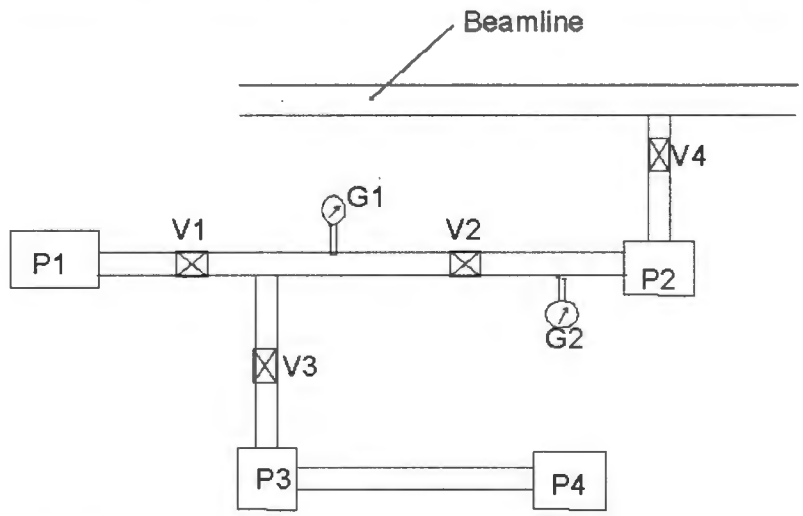

P1=Rotary vane Pump
P2=Diffusion Pump
P3=Turbo Molecular Pump
P4=Rotary Vane Pump
V=valve
G=gauge

3.4. Detector Performance Measurements

3.4.1. Assembling the System

Figure 3.4: Energy Spectrometry System

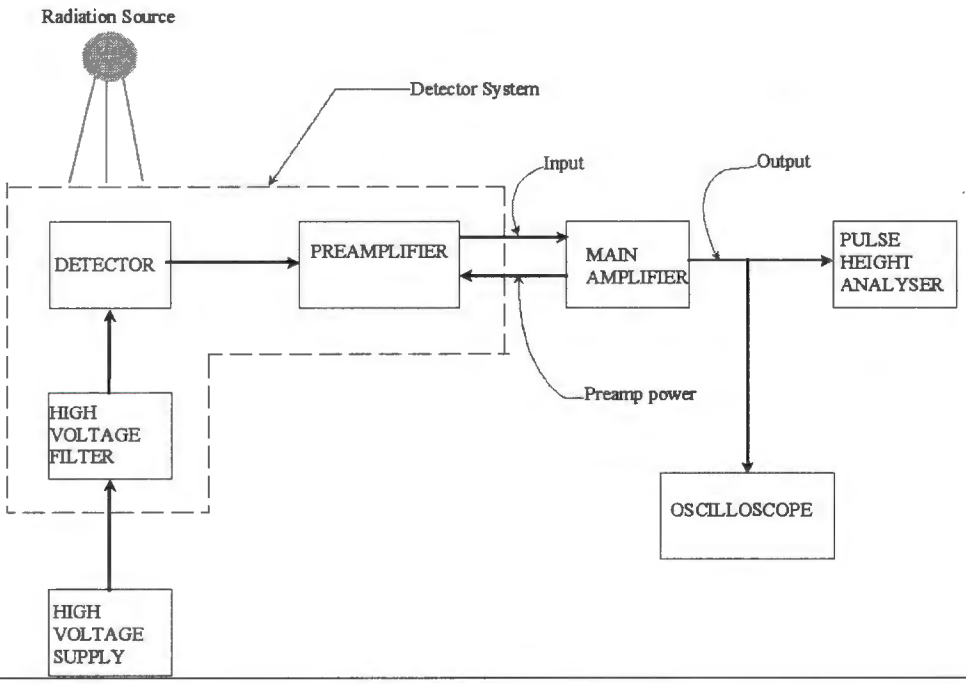

The liquid nitrogen Dewar of the detector was filled up and time was allowed to assure complete cooling of the detector element. The detector was then connected as part of the energy spectrometry system as shown in figure 3.4. Included were the detector with its attached amplifier and high voltage filter, main amplifier, multi-channel analyser, a detector, a bias supply, oscilloscope and computer.

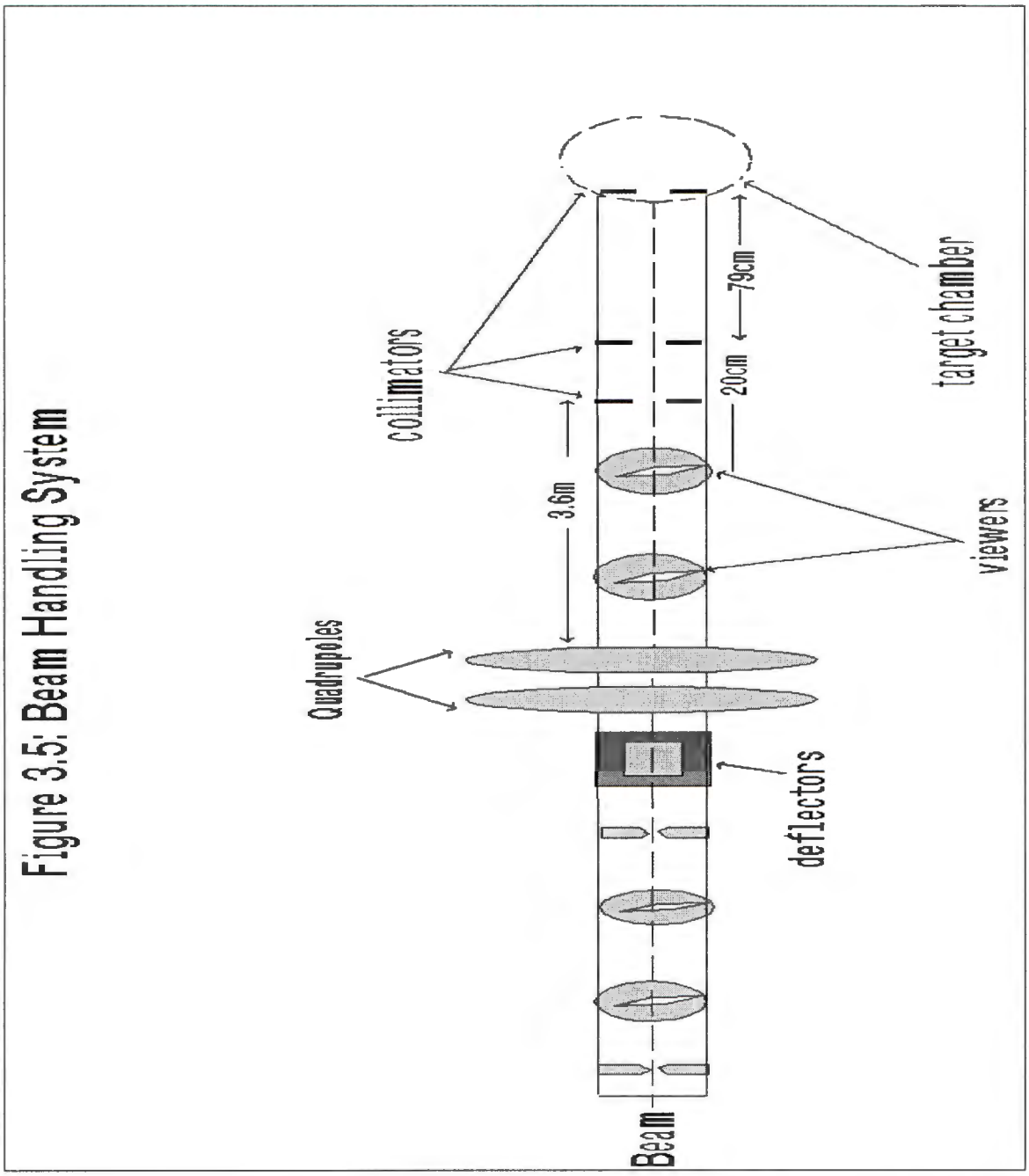

Figure 3.5: Beam Handling System

Connections between the preamplifier and the detector and between the high voltage filter and the detector were made through the cryostat vacuum feed-throughs within the electronics shield.

Detector bias (operating voltage) was furnished from the detector bias supply and

cabled to the detector's high voltage filter. The power cable from the preamplifier was attached to the preamplifier power connector on the main amplifier. The preamplifier output was connected to the input of the main amplifier. The unipolar output of the amplifier was connected to the oscilloscope and the bipolar output to the multichannel analyser (MCA). The MCA was connected to the computer.

3.4.2. Determination of Detector Resolution

3.4.2.1. HPGe (GLP Series) Detector

To determine the detector performance for low energy photons a 5.9 keV X-ray from ^{55}Fe source is used. ^{55}Fe source was placed in front of the Be window of the detector end-cap. The main amplifier gain was adjusted until the separation of the 5.9 keV and the 6.49 keV peaks were between 60 and 130 channels. The pole-zero of the amplifier was adjusted and the output was observed on the oscilloscope so that there was no distortion.

A spectrum was accumulated in the pulse height analyser using a computer program (EMCAPLUS). The system energy-slope was made in eV/channel from the two peaks(5.9keV and 6.49 keV).

The FWHM in channels was multiplied by the energy-slope calibration in eV/channel to find the system resolution in eV. This measured resolution was compared with the Quality Assurance Data Sheet for each detector.

3.4.2.2. HPGe(GMX Series) Detector

The same procedure as for the GLP detector except that the sources were different. Because of the versatility of the GMX detector, both ^{60}Co and ^{55}Fe were used to measure the resolution at a variety of energies (1.332MeV and 5.9 keV).

3.4.2.3. Si (Li) Detector

^{55}Fe source was used to measure the resolution at 5.9 keV.

3.5. Determination of Beam Profiles and Resolutions

A thin wire was used to scan the beam. When the proton beam stroke the wire, X-rays were produced from the wire. These X-rays were characteristic of the wire. A single peak was used to count the number of X-rays from the wire for each wire position. This produced a distribution of counts that were reflective of the distribution of the beam (see Figure 4.5 to 4.10).

3.6. Collimator Optimisation

Three collimator sets were inserted on the beamline to collimate the beam to the required size of beam diameter. The collimators were made of graphite and about 1mm thick. Starting with about 4mm diameter collimators, the collimators were aligned until the current integrator on the chamber wall showed a high reading of beam current.

When the beam current reached a maximum, smaller collimators were inserted and the alignment repeated. Various combinations of these sizes were attempted. The sizes of the collimators were reduced until the combination with the smallest sizes showed a reasonable alignment.

3.7. Determination of beam current

The target chamber served as the faraday cup. One current integrator was connected to the chamber wall and another to the collimator in the chamber. Both currents were read-off during the experiment to verify if the beam was hitting the target or not. If the beam hit the target, the current integrator on the chamber wall gave a higher reading. This was an indication that the beam was getting through, and the collimators were aligned.

A video camera, which was connected to the monitor, was placed in the control room to read the scale on the current integrator. The monitor was placed in the hall where

the experiments were carried out.

CHAPTER 4: RESULTS AND DISCUSSION

4.1. Beam Halo Investigation on old PIXE Beamline

Figure 4.1: Beam Halo Investigation on old PIXE Beamline

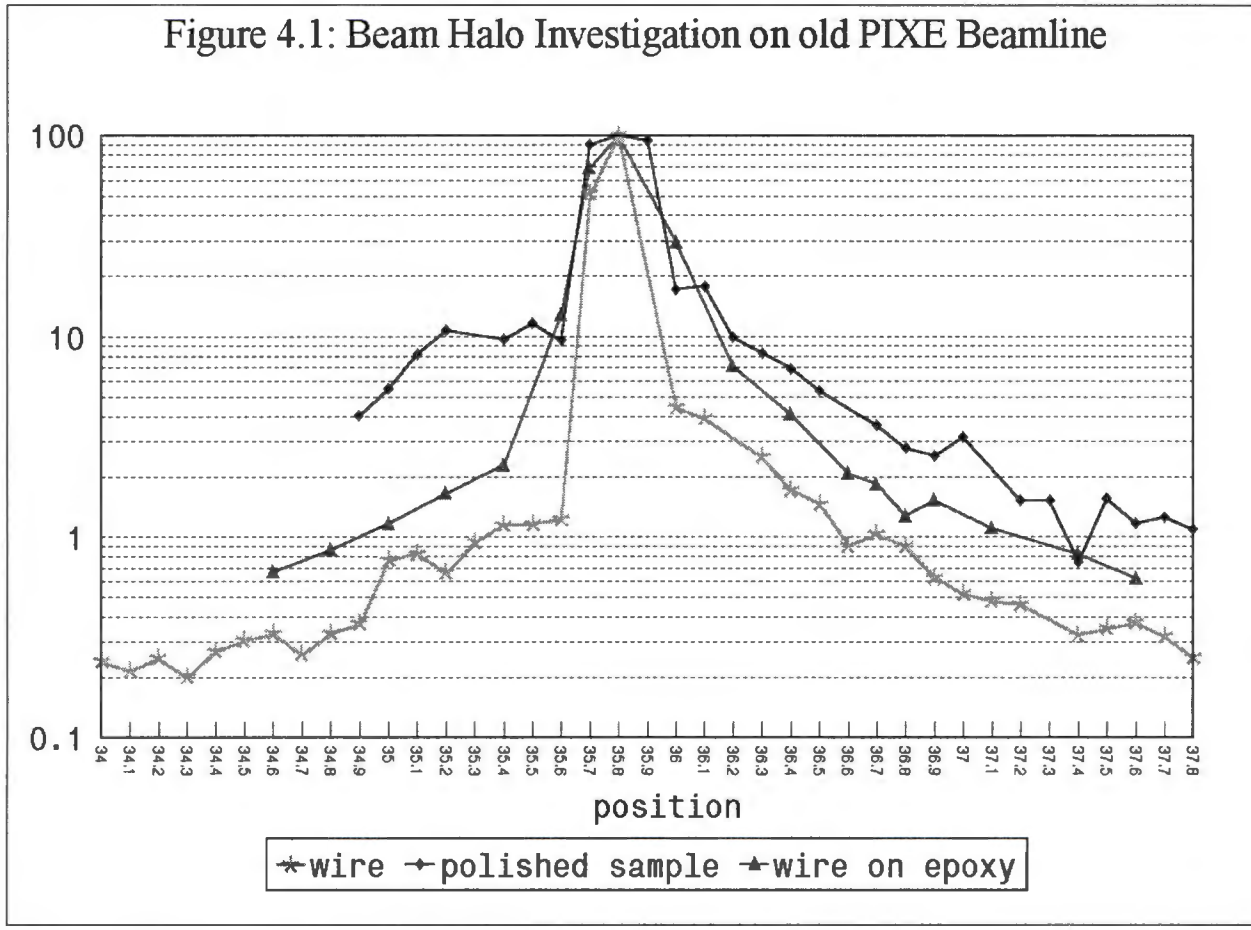

Figure 4.1 shows the distribution of counts plotted against the wire position. The beam distribution displays a halo with the intensity of the beam decreasing as the sample moves away from the beam centre. The beam profiles were not Gaussian distributions as expected. This might have resulted from the fluctuating beam current hence resulting in fluctuating counts of X-ray photons. The beam profiles are asymmetric and this is suspected to be the result of misalignment of the collimators

with respect to the beam.

The size of the beam was taken to be the Full Width at Half Maximum (FWHM) of profiles and results were tabulated in Table 4.4(a). The diameter of the wire on epoxy and polished sample are wider than that of the wire alone. For the wire on epoxy curve, the effect of broadening of the beam is associated with the backscattering of protons from the epoxy to the wire and producing more X-rays. This increases the counts around the edges of the wire and a wider beam is observed.

For the polished sample, counts are generally higher than both the wire on epoxy and wire alone. Some small quantities of material are suspected to spread over the surface during polishing of the sample and some X-rays are produced from these 'smears' to give more counts and broader beam.

4.2. New PIXE Beamline Set-up

It was difficult to align collimators in the new beamline (Figure 3.2) since they are very far apart. This can be deduced from Table 4.4(b). Generally the resolutions of the beam do not match the sizes of the collimators that are inserted. It was concluded that misalignment was present in the new beamline and resulted in small beam sizes and asymmetric beam profiles. Some beam sizes that were larger than collimator sizes were observed and were associated with beam broadening which is mainly caused by slit scattering.

Viewers have been inserted at different positions in the beamline to view the shape of the beam when it travels through the beam-tube. A desirable beam shape could be obtained while viewing and adjusting the quadrupole magnet settings. The quadrupoles could also be used for positioning and shaping the beam; thus directing a desirably shaped beam to the collimators.

4.3. Vacuum Pumps

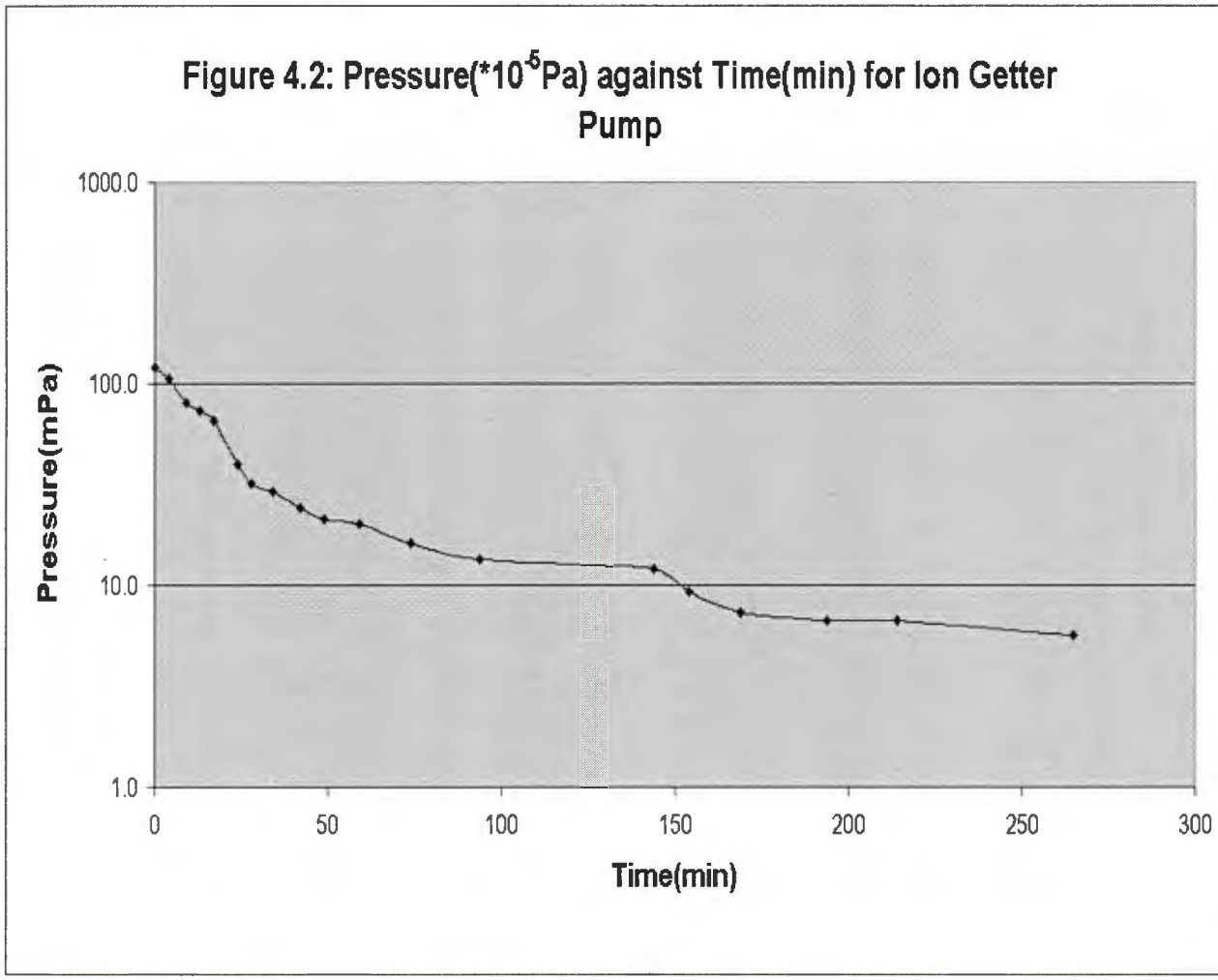

For each of the vacuum pumps tested, the results were plotted as shown in Figures

4.2, 4.3, and 4.4. All the vacuum pumps operated optimally during testing and were connected to the beamline as depicted on Figure 3.3. A vacuum in the range 10^{-6}–10^{-7}mbar can be achieved, but this could take longer time since the new beamline is long.

In general the pressure in the beamline drops gradually as the pumps are in operation. The getter ion pump is the most efficient pump since it pumps in the range of 10^{-6} mbar. All the pumps evacuate the beamline faster at the beginning of operation and stabilise as time progresses.

Figure 4.3:Variation of pressure with time for Oil Diffussion Pump

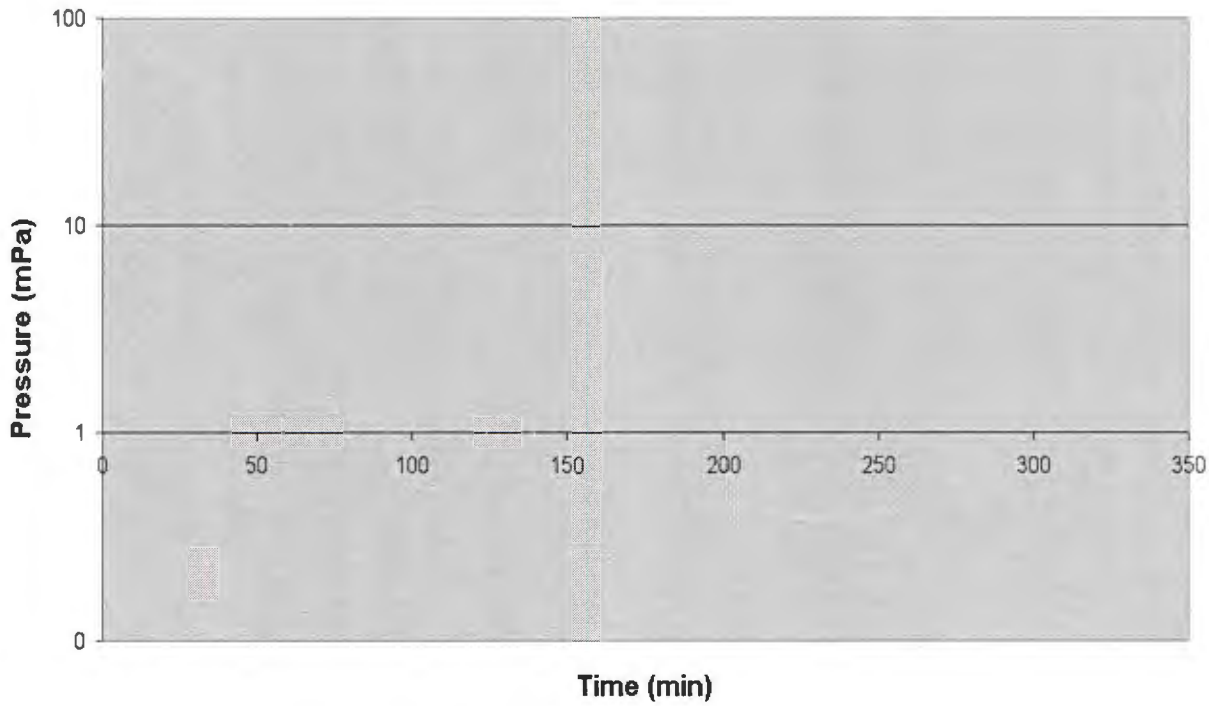

4.4. Detectors Resolution Measurements

When measuring detector resolutions, it is found that the count rate increases with as the source is brought closer to the detector. If the count-rate becomes very high the probability of pileup increases (see equation 2.9). In the old beamline, the Pileup Rejection Circuit (PURC) was used to reduce pileup effects for the optimisation of the quality of spectra. This will be required in the new beamline.

Table 4.1 Calibration of HPGe (GLP) Detector using ^{55}Fe Source

Distance (cm)	Energy (eV)	Count Rate (cps)	FWHM Resolution (eV)	Pulse Shaping Time (μs)
10	5892	18.9	177.25	6
15	5892	6.42	239.46	5
15	5892	6.4	238.02	4
15	5892	6.23	234.95	10
20	5892	3.73	247.19	6
20	5892	4.16	186.95	6
20	5892	1.62	214.85	6

The detector resolutions are dependent on the pulse shaping time, but there is no general trend to help in the selection of optimum pulse shaping time.

Table 4.2 Calibration of HPGe (GMX) Detector

Source	Distance (cm)	Energy (keV)	Count Rate (cps)	FWHM (eV)	Shaping Time (μs)
^{55}Fe	10	5.892	0.0363	266.76	5
^{55}Fe	15	5.892	1.30	563.13	5
^{60}Co	10	1332	1.28	2670	5
^{60}Co	20	1332	0.438	2530	5
^{60}Co	50	1332	0.113	2560	5

Table 4.3 Calibration of Si(Li) Detector

Energy (eV)	Count Rate (cps)	FWHM Resolution (eV)	Pulse Shaping Time (μs)
5892	2.27	190.3	12

Figure 4.4: Combination of OD, TM and RV Pumps

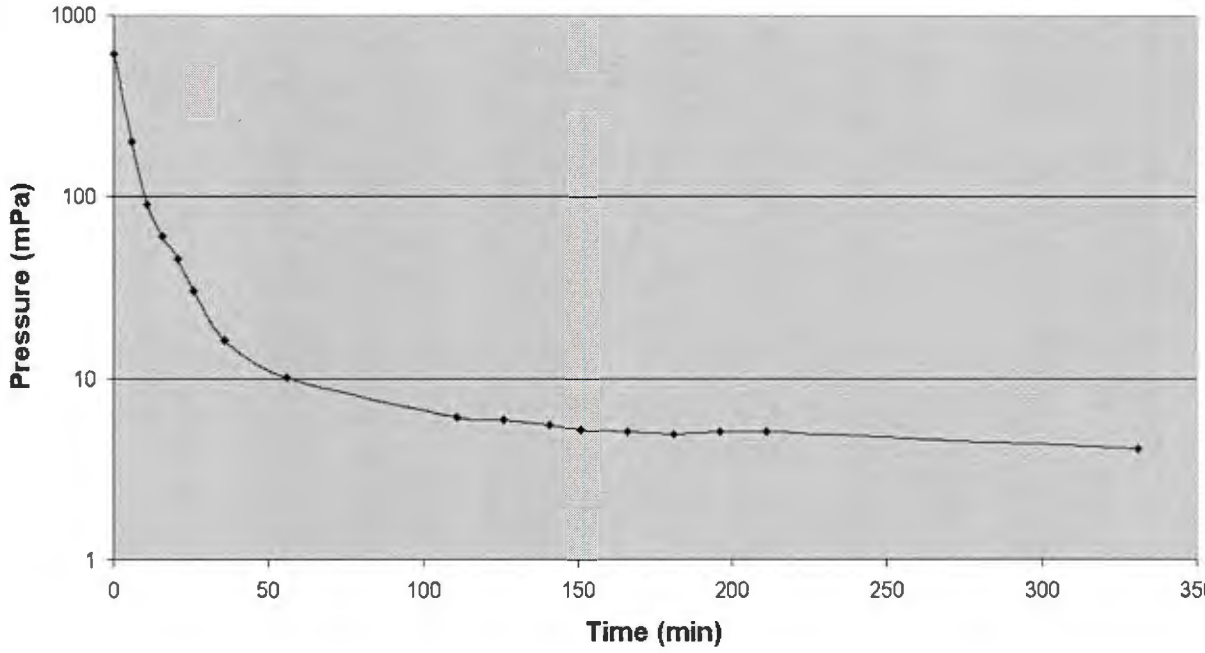

4.5. Beam Profiles and Resolutions

Figure4.5: 0.2, 0.2&0.15mm collimators

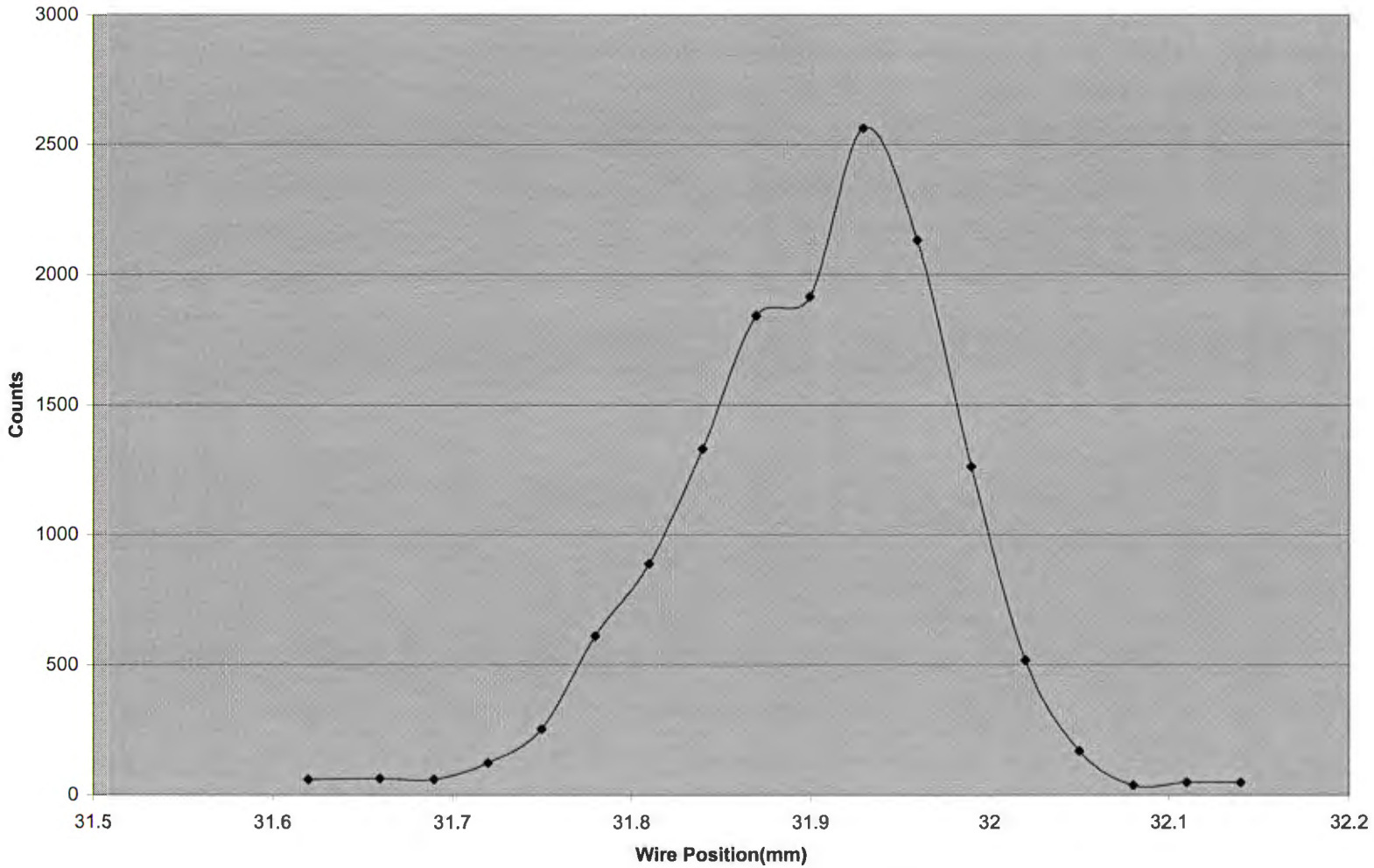

Figure 4.6: Profile for 0.1, 0.1mm collimator

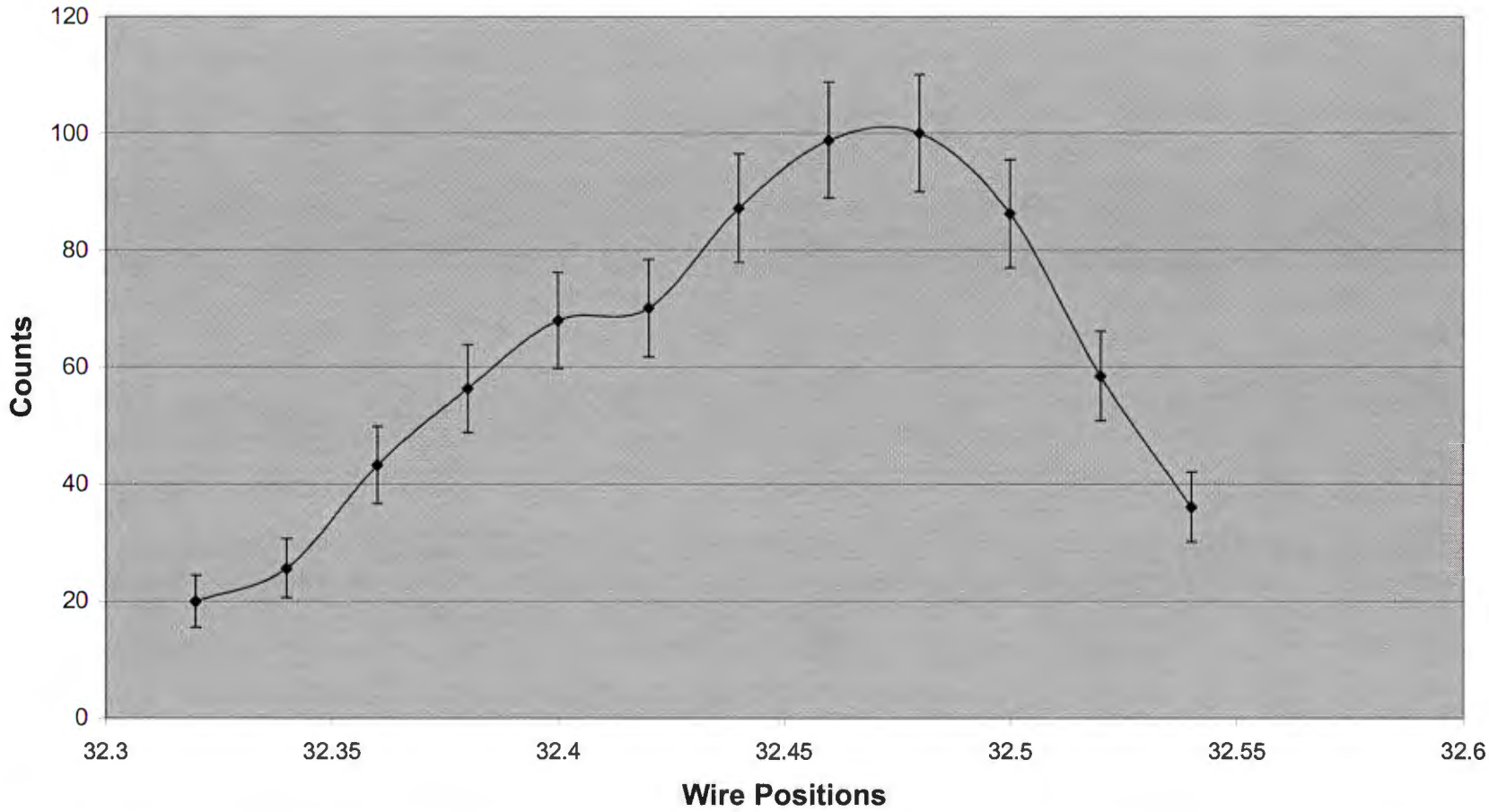

Figure4.7 for 0.1 & 0.15mm collimators

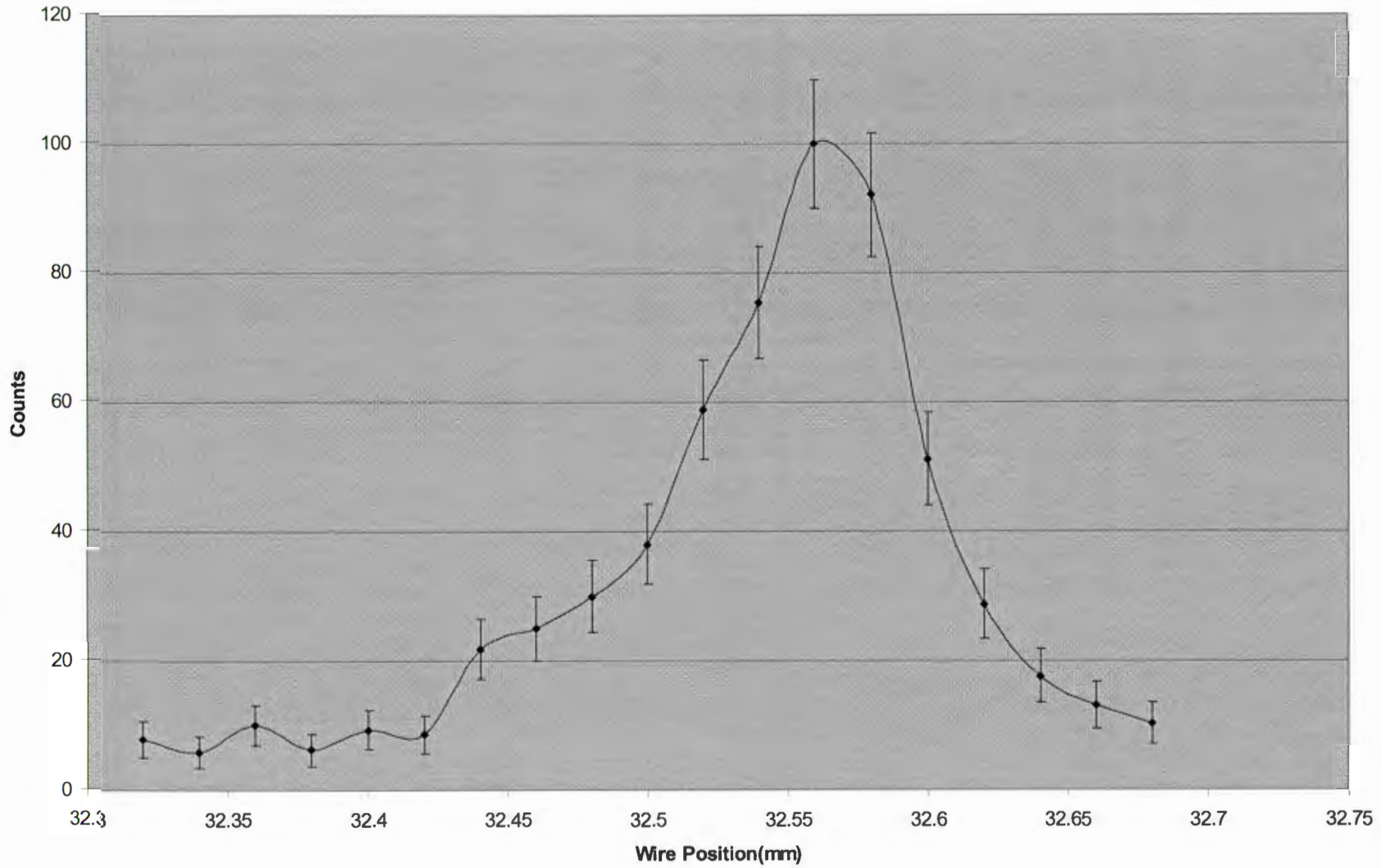

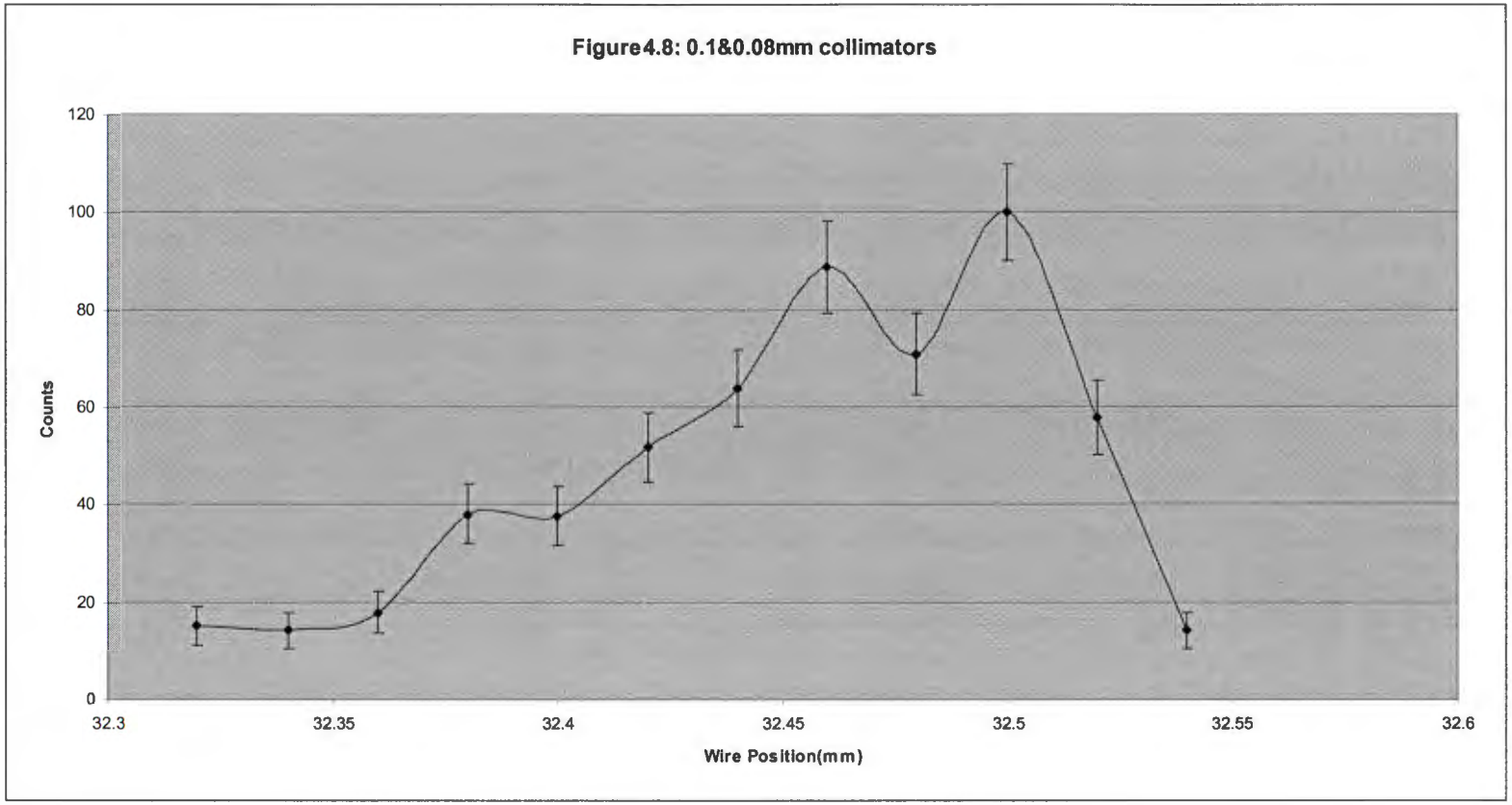
Figure4.8: 0.1&0.08mm collimators
120
100
80
60
40
20
0
Counts
32.3
32.35
32.4
32.45
32.5
32.55
32.6
Wire Position(mm)

Figure4.9: 0.1,1&0.15mm collimators

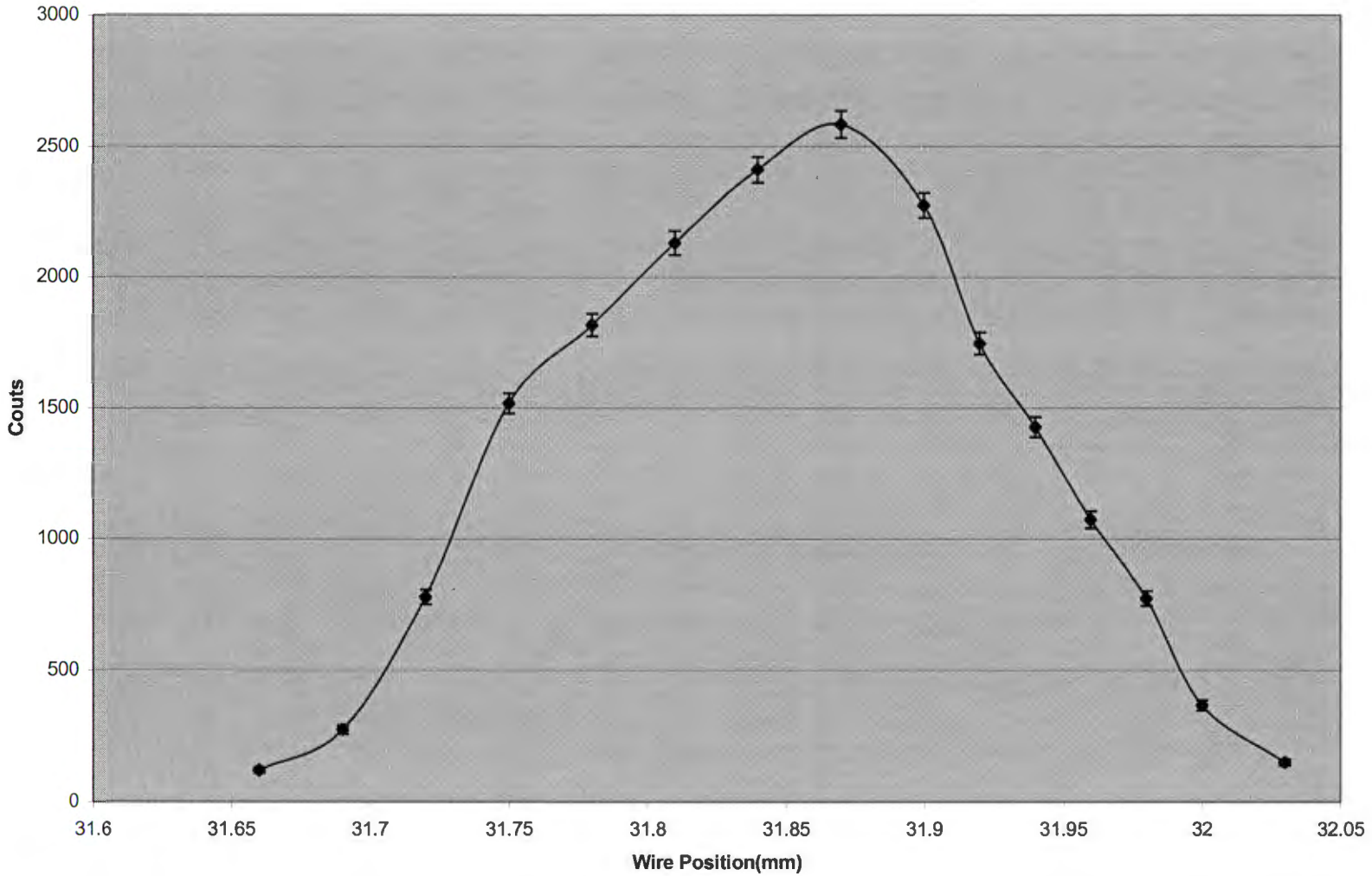

Figure4.10: 0.15, 0.15&2mm collimators

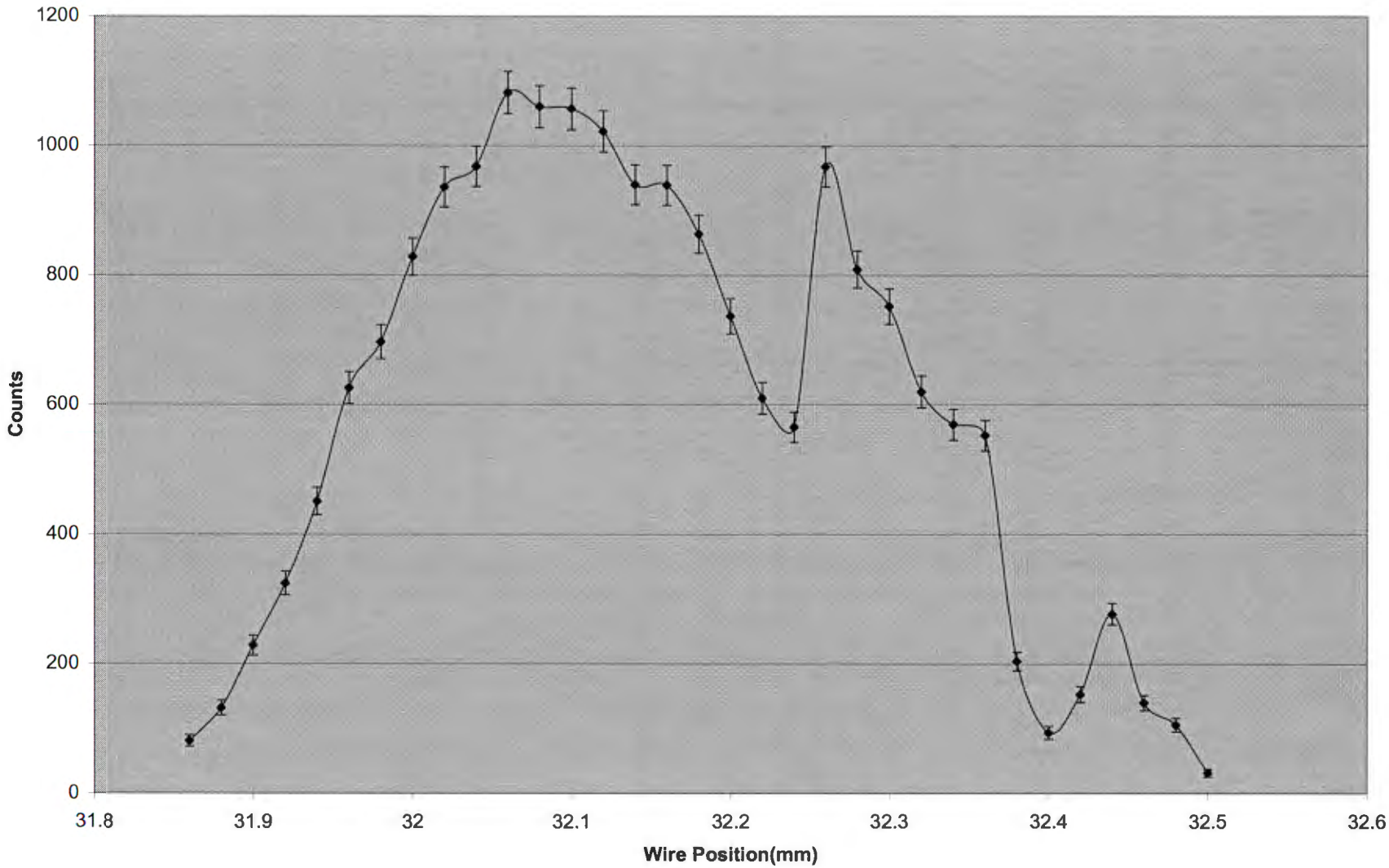

Table 4.4(a): Beam sizes on old PIXE beamline

Investigation	**wire**	**Wire on epoxy**	**Polished sample**
FWHM (μm)	**210**	**270**	**310**

Table 4.4(b) Collimator Combinations and their Resolutions

A (μm)	B (μm)	C (μm)	FWHM Resolution (μm)	Typical Beam Current (nA)
100	150	2000	90	0.05
100	80	2000	105	150
150	100	2000	129.27	-
150	200	150	137.93	0.03
150	150	2000	175	0.6
200	200	150	150	0.2
100	100	2000	157.5	-
150	1000	150	204	0.1

CHAPTER 5: SUMMARY AND CONCLUSION

Reasonable progress has been made in this work. The system has various modifications and has more future prospects for use when compared to the old one. This system will be suitable for many applications of micro-PIXE in geological studies since it meets most of the requirements. The main aim of obtaining a beam in the range of 40-80 micrometers was not achieved hence this system will require further development in this regard. Three sets of collimators have been used and this is hoped to minimise beam halo effects. The thickness of these collimators will help in reducing any transmission of protons through the edges.

It can be concluded that slit scattering is still taking place since there are resolutions showing a larger beam size even when collimators sizes are small. A false beam resolution might also be the result of slight misalignment of the collimators.

It is recommended that if all the offending sources of magnetic field can be removed, the problem of beam spot movement due to external magnetic fields could be solved.

Standards would be required to calibrate the system and check its reliability as a quantitative and qualitative analytical tool. This would confirm its applicability to elemental identification and Minimum Detection Limits.

It is hoped that the gold mines and platinum group metals (PGM) processors will benefit from the use of this facility.

REFERENCES

ALG82: M S A L Al-Ghazi et al, Nuclear Instruments and Methods 197 (1982) 117-120.

AVA90: L Avaldi et al, Nuclear Instruments and Methods B49 (1990), p24-28.

BAR84: Barfoot et al, Nuclear Instruments and Methods B5 (1984) 534.

BEU: G Beulich et al, X-ray Spectrometry, vol.28, 135-140.

BRO70: KL Brown(1962), SLAC75: Beam Transport Optics.

BUR62: EJ Burge and DA Smith, Rev. Sci. Instr.33 (1962) 1371.

CAH80: T A Cahill, Annual Review of Nuclear and Particle Science vol.30 (1980) p211-252.

CAM84: Campbell et al, Nuclear Instruments and Methods B5 (1984) 39.

COH81: DD Cohen, Nuclear Instruments and Methods B22(1981)p55.

COH87: DD Cohen and Clayton, Nuclear Instruments and Methods B22(1987)59.

COH89: DD Cohen and Clayton E (1989), Ion Beams for Materials Analysis, Academic Press, Australia.

GOC93: A A Gocharov et al, IEEE Transactions on Plasma Science vol.21 No.5 (1993).

JOH88: S A E Johansson (1988), PIXE: A Novel Technique for Elemental Analysis, John Wiley and Sons Ltd, Great Britain.

JOH86: S A E Johansson, Frezenius Z Analytical Chemistry vol.324 (1986) 635-641.

JOH92: S A E Johansson, Analyst vol.117 (1992) p259-265.

LEG97: G J F Legge, Nuclear Instruments and Methods B130(1997)p9-19.

LEE93: R W de Leeuw et al, Nuclear Instruments and Methods B83(1993)p284-290.

MAE97: M Maetz et al, Nuclear Instruments and Methods B130(1997)666-670.

MAK66: BK Mak, Nature 211(1966)738.

MAL82: K G Malmqvist et al, Journal of Radioanalytical Chemistry vol.74 No.1 (1982) 125- 147.

MON80: E C Montenegro et al, Nuclear Instruments and Methods 168(1980) p479-483.

MEO94: F Meot, Nuclear Instruments and Methods A340(1994)p594-604.

NOB75: R Nobilling et al, Nuclear Instruments and Methods 130(1975)325-334.

PAL96: J Pallon (1996), www.fysik.lu.se/~pixejan/PIXE.htm.

PIE66: TB Pierce et al, Nature 211(1966)66.

PRO89: VM Prozesky, 1989. Studies of interactions within silicon and germanium detectors. Pretoria: Atomic Energy Corporation of South Africa.124 p.

PRZ90: Przybylowicz W., Nuclear Instruments and Methods B50 (1990) 231.

SPI63: W S Spinks(1963), Vacuum Technology, Chapman and Hall, London.

SH79: Shima, Nuclear Instruments and Methods 165(1979).

STR91P: Strehl, Kerntechnik vol.56 (1991) No.4 p 208-213.

SIE93: S H Sie, Nuclear Instruments and Methods B75 (1993), p403-410.

SIE91: S H Sie et al, Nuclear Instruments and Methods B54 (1991) 284.

THI79: TP Thinh et al, X-Ray Spectrometry vol.8 (1979)p85.

THO77: Thornton et al, J Applied Physics, 48(1977) 1718.

TRA95: K Traxel et al, Nuclear Instruments and Methods B104(1995), p19-25.

WAT95: F Watt et al, Nuclear Instruments and Methods B104 (1995) 101-106.

ZIE85: JF Ziegler(1985), Stopping Powers and Ranges of Ions vol.1, Pergamon, New York.